



HAL
open science

Microphysics impacts on the warm conveyor belt and ridge building of the NAWDEX IOP6 cyclone

Marie Mazoyer, Didier Ricard, Gwendal Rivière, Julien Delanoë, Philippe Arbogast, Benoit Vié, Christine Lac, Quitterie Cazenave, Jacques Pelon

► To cite this version:

Marie Mazoyer, Didier Ricard, Gwendal Rivière, Julien Delanoë, Philippe Arbogast, et al.. Microphysics impacts on the warm conveyor belt and ridge building of the NAWDEX IOP6 cyclone. Monthly Weather Review, 2021, (in press). 10.1175/MWR-D-21-0061.1 . insu-03381560v1

HAL Id: insu-03381560

<https://insu.hal.science/insu-03381560v1>

Submitted on 18 Oct 2021 (v1), last revised 9 Dec 2021 (v2)

HAL is a multi-disciplinary open access archive for the deposit and dissemination of scientific research documents, whether they are published or not. The documents may come from teaching and research institutions in France or abroad, or from public or private research centers.

L'archive ouverte pluridisciplinaire **HAL**, est destinée au dépôt et à la diffusion de documents scientifiques de niveau recherche, publiés ou non, émanant des établissements d'enseignement et de recherche français ou étrangers, des laboratoires publics ou privés.

1 **Microphysics impacts on the warm conveyor belt and ridge building of the**
2 **NAWDEX IOP6 cyclone**

3 Marie Mazoyer *

4 *CNRM, Université de Toulouse, Météo-France, CNRS, Toulouse, France*

5 Didier Ricard

6 *CNRM, Université de Toulouse, Météo-France, CNRS, Toulouse, France*

7 Gwendal Rivière

8 *LMD/IPSL, École Normale Supérieure, PSL Research University, École Polytechnique, Sorbonne*

9 *Universités, CNRS, Paris, France*

10 Julien Delanoë

11 *LATMOS-IPSL, CNRS/INSU, University of Versailles, Guyancourt, France*

12 Philippe Arbogast

13 *CNRM, Université de Toulouse, Météo-France, CNRS, Toulouse, France*

14 Benoit Vié

15 *CNRM, Université de Toulouse, Météo-France, CNRS, Toulouse, France*

16 Christine Lac

17 *CNRM, Université de Toulouse, Météo-France, CNRS, Toulouse, France*

18

Quitterie Cazenave

19

LATMOS-IPSL, CNRS/INSU, University of Versailles, Guyancourt, France

20

Jacques Pelon

21

LATMOS-IPSL, CNRS/INSU, University of Versailles, Guyancourt, France

²² *Corresponding author: Marie Mazoyer, marie.mazoyer@meteo.fr

ABSTRACT

23 This study investigates diabatic processes along the warm conveyor belt (WCB) of a deep extra-
24 tropical cyclone observed of the North Atlantic Waveguide and Downstream Impact Experiment
25 (NAWDEX). The aim is to investigate the effect of two different microphysics schemes, the one-
26 moment scheme ICE3 and the quasi two-moment scheme LIMA, on the WCB and the ridge building
27 downstream. ICE3 and LIMA also differ on the processes of vapor deposition on hydrometeors in
28 cold and mixed-phase clouds. Latent heating in ICE3 is found to be dominated by deposition on
29 ice while the heating in LIMA is distributed among depositions on ice, snow and graupel. ICE3
30 is the scheme leading to the largest number of WCB trajectories (30% more than LIMA) due to
31 greater heating rates over larger areas. The consequence is that the size of the upper-level ridge is
32 growing more rapidly in ICE3 than LIMA, albeit with some exceptions in localized regions of the
33 cyclonic branch of the WCB. A comparison with various observations (airborne remote sensing
34 measurements, dropsondes and satellite data) is then performed. Below the melting layer, the ob-
35 served reflectivity is rather well reproduced by the model. Above the melting layer, in the middle of
36 the troposphere, the reflectivity and retrieved ice water content are largely underestimated by both
37 schemes while at upper levels, the ICE3 scheme performs much better than LIMA in agreement
38 with a closer representation of the observed winds by ICE3. These results underline the strong
39 sensitivity of upper-level dynamics to ice related processes.

40 **Plain Language Summary**

41 In mid-latitudes, the jet stream structure is modulated by diabatic processes occurring in the warm
42 conveyor belt of extratropical cyclones. By using two drastically different microphysical schemes
43 to simulate an extratropical cyclone, we investigate the main cloud processes and associated
44 uncertainties mattering to represent the warm conveyor belt. Comparison with data from the
45 NAWDEX campaign helps to determine the most accurate scheme. We highlight the strong
46 sensitivity of upper-level dynamics to ice related processes. These findings point out the need of a
47 better understanding of these processes for an improved prediction of upper-level dynamics.

48 **1. Introduction**

49 Extratropical cyclones result from complex interactions between synoptic-scale dynamical forc-
50 ings and micro-scale physical processes and are still subject to significant prediction errors in
51 Numerical Weather Prediction models (NWP). Warm Conveyor Belts (WCB) are key regions of
52 extratropical cyclones where these multi-scale complex interactions occur. According to Eckhardt
53 et al. (2004), in the Northern Hemisphere, $\sim 60\%$ of the extratropical cyclones are associated
54 with WCB and their deepening rate is linked to the WCB strength (Binder et al. 2016). WCBs
55 correspond to slantwise ascending air masses originating in the boundary layer of the warm sector
56 and reaching the upper troposphere (Harrold 1973; Browning 1986). Within the troposphere,
57 they form elongated cloud bands and horizontally transport large amounts of heat and moisture
58 (Holton 2004). During their ascent, liquid, mixed phase, and ice hydrometeors are formed in
59 WCBs (Browning 1986).

60 Microphysical water phase changes associated with cloud formation along WCBs have been
61 shown to have a strong impact on cyclone intensity (Manabe 1956; Robertson and Smith 1983,
62 among many others) and cyclone track (Coronel et al. 2015). These impacts can be viewed in terms

63 of Potential Vorticity (PV). The time evolution of the PV depends on the spatial gradient of the
64 diabatic heating rate (Hoskins et al. 1985). In WCBs, microphysical processes generally produce
65 latent heat release larger than 20 K in 48 h (Madonna et al. 2014). Such a latent heat release
66 produces a positive PV anomaly in the lower troposphere which generally reinforces the cyclonic
67 circulation of the surface extratropical cyclones (Kuo et al. 1991; Davis et al. 1993; Binder et al.
68 2016). The latent heat release also creates a negative PV anomaly in the upper troposphere that
69 tends to reinforce the downstream ridge (Hoskins et al. 1985; Wernli and Davies 1997; Pomroy
70 and Thorpe 2000; Madonna et al. 2014). This upper tropospheric PV anomaly has a strong impact
71 on the downstream propagation of Rossby waves and consequently on the forthcoming weather.
72 Several studies have shown that NWP models are often characterized by a misrepresentation of the
73 PV along the jet stream (Dirren et al. 2003; Gray et al. 2014; Martínez-Alvarado et al. 2016) whose
74 origins might be diabatic processes, and in particular the cloud microphysical processes within
75 WCBs. These previous studies helped motivate the international field campaign NAWDEX (North
76 Atlantic Waveguide Downstream and impact EXperiment) which was conducted in September-
77 October 2016 (Schäfler et al. 2018).

78 The most significant microphysical processes along WCBs are associated with condensation of
79 cloud liquid water, depositional growth of snow and ice, and snow riming as shown by various
80 studies (Forbes and Clark 2003; Joos and Wernli 2012; Joos and Forbes 2016; Dearden et al.
81 2016; Crezee et al. 2017; Gehring et al. 2020). Cloud systems have been shown to be highly
82 dependent on the way ice vapor growth is parameterized (Gierens et al. 2003; Tompkins et al.
83 2007; Avramov and Harrington 2010) but uncertainties on ice related processes are still large
84 (Khain et al. 2015; Dearden et al. 2016). In warm clouds, all the excess vapor is removed by
85 a saturation adjustment scheme. In cold and mixed clouds, saturation adjustment is also often
86 used. However, ice number concentration is several orders smaller than cloud droplets number

87 concentration and supersaturation reached in cold and mixed clouds is far higher than in warm
88 clouds and the assumption of saturation adjustment is no longer applicable (Heymsfield et al. 1998;
89 Gettelman et al. 2010). When the ice-saturation adjustment is applied, the excess water vapor in
90 the upper troposphere is entirely consumed to produce large amount of cloud ice and subsequently
91 releases large amount of latent heating (Hashimoto et al. 2007). By doubling or halving the ice
92 deposition rate in a mesoscale version of the Met Office Unified Model, Forbes and Clark (2003)
93 observed significant impacts on the dynamics of a cyclone and its fronts but, due to the absence
94 of microphysics observations, the authors could not state on the best deposition rate and they did
95 not look at the representation of the PV along the jet stream. Joos and Forbes (2016), while using
96 different microphysics differing on accretion, rain evaporation and snow riming, detected small
97 changes in the structure and location of the WCB that have some impact on the position of the
98 tropopause and extension of the upper-level ridge. However, these differences in microphysics did
99 not lead to differences in the number of WCB trajectories. Extratropical cyclones are complex
100 systems and the underlying interactions between microphysics and dynamics within WCB may
101 potentially lead to forecast uncertainties along the downstream waveguide (Berman and Torn
102 2019). However, it is still unclear to which components of the microphysical schemes along WCB
103 trajectories the downstream waveguide is more sensitive.

104 The main objective of the present study is to assess the impact of different microphysics on
105 the development of an extratropical cyclone and its associated ridge building aloft in the French
106 mesoscale research model Meso-NH (Lac et al. 2018). Two largely different microphysics schemes
107 are compared: the one-moment microphysical scheme ICE3 (Pinty and Jabouille 1998) and the
108 quasi two-moment microphysical scheme LIMA (Liquid Ice Multiple Aerosols, Vié et al. (2016)).
109 Since the cyclone has been observed during the Intensive Observing Period 6 (IOP6) of NAWDEX,

110 a subsequent secondary objective is to determine which of the scheme performs better with regard
111 to observations.

112 The one-moment scheme ICE3 is currently used in AROME (Seity et al. 2011), the operational
113 regional NWP model at Météo-France. It describes the evolution of the mass mixing ratio of five
114 different hydrometeors (droplets, rain, graupel, snow and ice). The quasi two-moment scheme
115 LIMA describes the evolution of both the mass mixing ratios and number concentrations of the
116 same five hydrometeors. These schemes also differ on the processes of vapor deposition on ice
117 hydrometeors in cold and mixed clouds. For instance, ICE3 uses ice-saturation adjustment while
118 LIMA predicts explicit rates of water vapor deposition.

119 Such a comparison between the two schemes has already been performed in a very different
120 context on two heavy precipitation events of the HyMeX campaign (Ducrocq et al. 2014) by
121 Taufour et al. (2018). The one-moment scheme produced higher values of hydrometeor mass
122 mixing ratio. This could be due inter alia to higher vapor deposition rates or to lower sedimentation
123 speeds. But the two-moment scheme obtained a closer vertical composition of the convective cells
124 to the observations. This last point might be relevant in our case as Rasp et al. (2016), Oertel et al.
125 (2020) and Blanchard et al. (2020) recently showed the particular roles of embedded-convection in
126 creating upper-level negative PV bands on the anticyclonic side of the jet stream and reinforcing it.

127 The case studied in this paper is called the "Stalactite Cyclone" due to a very deep, narrow,
128 stalactite-like tropopause trough associated with it following the analogy introduced by Rossa et al.
129 (2000). This case is particularly interesting to study because its associated ridge building led to
130 the onset of a synoptic-scale Scandinavian blocking in early October 2016 (Schäfler et al. 2018;
131 Maddison et al. 2019). It has been observed during three aircraft flights: two flights of the French
132 Falcon operated by SAFIRE (Service des Avions Français Instrumentés pour la Recherche en

133 Environnement) and one flight of the German Falcon operated by the DLR (Deutsches Zentrum
134 für Luft- und Raumfahrt).

135 The structure of the paper is as follows. Section 2 is dedicated to the description of the NAWDEX
136 case study and the methodology. It first includes information about the model and its detailed bulk
137 microphysical schemes ICE3 and LIMA. It also includes a synoptic overview of the NAWDEX
138 case study and a description of the observational datasets. The impact of the two schemes on the
139 WCB of the studied cyclone and the building of the upper-level ridge are then described in section
140 3. Section 4 is dedicated to the comparison to airborne in-situ and radar-lidar observations of
141 microphysics and dynamics in an attempt to assess the effect of the microphysical schemes on the
142 skill of the NWP model in the case studied here. Discussions and conclusions are drawn in section
143 5.

144 **2. Case description and methodology**

145 *a. NAWDEX IOP 6*

146 The "Stalactite Cyclone" which formed during IOP 6 of NAWDEX is selected for our study and
147 corresponds to the beginning of sequence B as depicted in Schäfler et al. (2018) (e.g., see their
148 Fig. 6). The initial cyclogenesis occurred off the coast of Newfoundland by the merging of two
149 small-scale vortices on 29 September 2016 (Flack et al. 2021). An interaction with a large-scale
150 upper-level trough over the North Atlantic led to a rapid deepening of the surface cyclone by 26
151 hPa in 24h. Figure 1 presents the track of the cyclone obtained with the global operational model
152 ARPEGE analysis from 00 UTC 1 October to 00 UTC 4 October every 6 hours (black line in
153 Fig. 1a). The cyclone was associated with a strong WCB that amplified the upper level ridge
154 downstream of it (Figs. 1b-d). On 4 October the ridge led to a blocking situation that persisted over

155 Scandinavia for several weeks (Schäfler et al. 2018; Maddison et al. 2019). Two flights with the
156 French SAFIRE Falcon were conducted during the development of the cyclone and its associated
157 WCB on 2 October (see flights tracks in Fig. 1b). The first one, called F6, lasted from 0837 UTC
158 to 1150 UTC and sampled the WCB outflow region west of Iceland. The second one, called F7,
159 which lasted from 1301 to 1616 UTC, sampled the ascending branch of the WCB south of Iceland.

160 *b. French NAWDEX airborne observations and comparison with model outputs*

161 During NAWDEX, the French SAFIRE Falcon was equipped with a radar-lidar platform (RALI;
162 <http://rali.projet.latmos.ipsl.fr/>, Delanoë et al. 2013). It includes a multi-beam 95 GHz Doppler
163 radar RASTA (RAdar SysTem Airborne), a high-spectral-resolution LNG (Leandre New Gener-
164 ation) lidar, and an infrared radiometer CLIMAT (Conveyable Low-Noise Infrared Radiometer
165 for Measurements of Atmosphere and Ground Surface Targets; Brogniez et al. 2003). RASTA
166 includes 3 downward-looking beams (nadir, 28 degrees off-nadir and opposite the aircraft motion,
167 and 20 degrees off-nadir perpendicular to the aircraft motion). This unique configuration allows
168 for the retrieval of the three-dimensional wind. LNG, in its backscatter configuration, operates at
169 three wavelengths (355 nm, 532 nm, 1064 nm), including depolarization at 355 nm.

170 Two complementary approaches are adopted to compare the simulations and the observations:
171 the radar-to-model approach, which consists of deriving usual meteorological parameters such
172 as hydrometeor contents from radar-lidar measurements, and the model-to-radar approach, which
173 simulates the reflectivity from the model fields. Both approaches have their own assumptions on
174 hydrometeor shape, density, etc. The model-to-radar approach relies on a radar forward operator
175 developed within Meso-NH following the Mie scattering theory. The simulated reflectivity can be
176 compared to the reflectivity measured by a fixed ground-based radar (Caumont et al. 2006; Augros
177 et al. 2016) or by one measured along a flight track (Borderies et al. 2018). The radar sensitivity

178 depending on the range of the target (e.g., RASTA sensitivity is about -30 dBZ at 1 km range) the
179 radar cannot detect the very low values shown in the model simulations. Consequently only the
180 range of observed values are considered for comparison purposes. Therefore, at each altitude, the
181 simulated reflectivity values that are smaller/larger than the minimum/maximum of the instrument
182 range are excluded. In the latter study, the operator has been validated by comparisons with the
183 RASTA data during a 2-month period over the Mediterranean region. The radar-to-model approach
184 is based on the DARDAR-CLOUD algorithm (Delanoë et al. 2013; Cazenave 2019) which enables
185 the retrieval of microphysical properties from the RALI data using T-matrix scattering theory
186 (Mishchenko et al. 1996) such as the ice water content, the effective radius, and the extinction.
187 Adopting these two complementary and independent approaches, which are based on different
188 assumptions and exploitation algorithms, reinforces the robustness of our comparisons between
189 observations and models and constitutes one originality of the present study.

190 Nine dropsondes were launched during F6 that provided temperature, humidity and wind profiles.
191 During F7, no dropsonde was launched because of the air traffic constraints. Finally, to get a fair
192 comparison with the observations, Meso-NH simulations are systematically interpolated in time
193 and space at the exact position of the observations.

194 *c. Model and simulation setup*

195 This study uses the French anelastic research model Meso-NH (Mesoscale Non-Hydrostatic)
196 (Lac et al. 2018, <http://mesonh.aero.obs-mip.fr/>). The Meso-NH prognostic variables are the three
197 velocity components, the dry potential temperature, the turbulent kinetic energy and the micro-
198 physical variables. Meso-NH was used in a convection-permitting mode at a 2.5 km horizontal
199 resolution over the domain shown in Figs. 1a-d. The vertical grid included 55 stretched vertical
200 levels with the first one 20 m above the ground. The momentum is advected with a fourth-order

201 centered scheme, while scalar variables are advected with the Piecewise Parabolic Method (PPM)
202 scheme (Colella and Woodward 1984). The time step is 6 s with a Runge-Kutta fourth-order
203 temporal scheme. The turbulence scheme is the 1-D version of Cuxart et al. (2000) used with the
204 mixing length of Bougeault and Lacarrere (1989) and the mass-flux scheme of Pergaud et al. (2009).
205 The radiative transfer is computed with the ECMWF radiation code, using the Rapid Radiation
206 Transfer Model (RRTM) of Mlawer et al. (1997) for longwave radiation and the shortwave radiation
207 scheme of Morcrette (1991). In Meso-NH backward Lagrangian trajectories are calculated using
208 the online algorithm of Gheusi and Stein (2002). The tracers are initialized with their initial 3-D
209 coordinates and are transported by PPM, a scheme with excellent mass-conservation properties
210 and low numerical diffusion. Two distinct simulations are performed in this study, the first uses
211 the microphysical parameterization scheme ICE3 and the second LIMA. In what follows these
212 simulations are referred to as ICE3 and LIMA simulations.

213 1) ICE3 MICROPHYSICAL SCHEME

214 ICE3 is a bulk mixed-phase one-moment microphysical scheme (Caniaux et al. 1994; Pinty and
215 Jabouille 1998). Its prognostic equations predict the mass mixing ratios of six water species (water
216 vapor, cloud water, rainwater, primary ice crystals, snow aggregates, and graupel) combining a
217 three-class ice parameterization with the Kessler (1969) scheme applied to the warm processes.
218 The total number concentration of the cloud droplets is defined according to the fraction of sea and
219 land surface cover of the grid mesh, with $300 \times 10^6 \text{ m}^{-3}$ particles over land and $100 \times 10^6 \text{ m}^{-3}$ over
220 sea. The total number concentration of the primary ice is diagnosed based on the parameterization
221 of heterogeneous nucleation of Meyers et al. (1992), which depends only on the supersaturation.
222 An adjustment to saturation for liquid/solid phase is performed meaning that there is deposition of
223 all the excess vapor on cloud droplets/ice particles in warm/cold clouds. In mixed-phase clouds, a

224 barycentric formula based on ice and cloud droplets mass mixing ratio is used to divide the excess
225 vapor between ice particles and cloud droplets, which may lead to artificial distribution between
226 hydrometeors. Ice to snow conversion is performed according to Kessler (1969) and depends
227 on the ice mass mixing ratio and on the temperature. In cold clouds, snow is only formed by
228 autoconversion and aggregation of ice while graupel is first formed by riming and can then grow
229 by collecting ice and snow. ICE3 includes a subgrid condensation scheme in which the cloud
230 scheme considers saturation deficit according to Chaboureau and Bechtold (2002) and the shallow
231 convection scheme of Pergaud et al. (2009).

232 2) LIMA MICROPHYSICAL SCHEME

233 LIMA (Liquid Ice Multiple Aerosols; Vié et al. 2016)¹ is a quasi two-moment scheme that
234 includes a detailed representation of aerosol-cloud interactions. LIMA inherits the six water
235 species of the ICE3 scheme. In addition to the mass mixing ratio, and through aerosols
236 consideration, it predicts the number concentration of the cloud droplets, raindrops and pristine
237 ice crystals. As concentrations of snow and graupel are diagnostic, we use the term of quasi
238 2 moment scheme. The LIMA scheme integrates a prognostic representation of the aerosol
239 population. Cloud Condensation Nuclei (CCN) activation is parameterized following Cohard
240 et al. (1998). Ice Freezing Nuclei (IFN) nucleation is parameterized according to Phillips et al.
241 (2008) but revised as in Phillips et al. (2013). IFN nucleation explicitly depends on the surface
242 properties of glaciogenic aerosols. In our simulations, the CCN number concentration is set
243 to $300 \times 10^6 \text{ m}^{-3}$ between the ground and a height of 1 000 m. Above 1 000 m, the number
244 concentration decreases exponentially up to 10 000 m where it reaches a constant value of
245 $10 \times 10^3 \text{ m}^{-3}$. The IFN number concentration is homogeneous and set to 10 m^{-3} . Sensitivity

¹Technical note on LIMA at http://mesonh.aero.obs-mip.fr/mesonh54/BooksAndGuides?action=AttachFile&do=view&target=scidoc_p3.pdf

246 tests to CCN and IFN number concentrations have been performed with very little impact on the
247 simulations. As in ICE3, for the warm phase there is condensation of all the excess vapor on
248 cloud liquid water. However, for the cold phase the deposition rate is explicitly predicted for ice,
249 snow and graupel. In mixed-phase clouds, an adjustment to liquid water saturation first prevents
250 supersaturation, and then the simultaneous evolution of droplets and ice crystals is parame-
251 terized after Reisin et al. (1996) and an explicit mass transfer rate on snow and graupel is computed.

252

253 In opposition to ICE3:

- 254 • No adjustment to saturation is made on solid phase and some vapor can stay in excess in the
255 cold and mixed phases.
- 256 • Snow and graupel can grow by vapor deposition in the cold clouds.
- 257 • No subgrid condensation scheme is used.

258 These points are very relevant as, at each time step, mass is transferred between the 6 water
259 species (vapor, ice, snow, graupel, rain and droplets) such that a change of phase occurs and latent
260 heat is released/consumed.

261 A previous comparison between these two schemes performed on heavy precipitation events
262 Taufour et al. (2018) noticed several significant differences. LIMA was found to be more skillful
263 in various ways: it produced a more realistic rain mass mixing ratio, a better representation of
264 the hydrometeors contents as function of height, and an improvement of the representation of the
265 hydrometeors contents in convective areas and the cloud tops. They also observed that LIMA
266 produced more snow than ICE3 but less graupel and far less pristine ice (see their Fig. 8).

267 3) INITIAL CONDITIONS, SYNOPTIC OVERVIEW AND LAGRANGIAN TRAJECTORIES SEEDING

268 The simulations are initialized at 00 UTC 1 October 2016 and last 72 hours. Initial and lateral
269 boundary conditions are provided by 6-hourly ARPEGE analyses. At the initial time the cyclone is
270 located in the southwestern part of the Meso-NH domain and the upper-level ridge to the east of the
271 surface cyclone is partly formed and covers a large part of the Meso-NH domain (Figs. 1a-b). The
272 tracks of the cyclone, as simulated by ICE3 and LIMA, are almost superimposed on each other and
273 slightly more to the east compared to ARPEGE analysis (Fig. 1a). At the end of the simulations,
274 on 4 Oct, the surface low is not further deepening, while the ridge is amplifying further to the north
275 (not shown). The following results focus on the first 2 days of the simulations when the cyclone
276 keeps deepening and the ridge amplifies the most.

277 Seeding of backward trajectories is made at 00 UTC 3 October only when the differences between
278 ICE3 and LIMA are already large enough. Information on trajectories is given every 15 minutes on
279 a $2.5 \text{ km} \times 2.5 \text{ km}$ horizontal grid over the domain shown in Fig. 1. Due to the high computational
280 cost, only one point over eight is considered in the horizontal directions. In the vertical direction
281 all the 22 levels are seeded from 3 600 m to 14 400 m.

282 **3. Microphysics properties and latent heating budget along the warm conveyor belt**

283 Different criteria can be applied to identify WCB trajectories. This study follows Joos and Wernli
284 (2012) and uses a criterion that requires an ascent of more than 600 hPa in 48 h. A significant
285 difference in the number of WCB trajectories are found between the two runs: ICE3 has 10 475
286 trajectories whereas LIMA 7 945 trajectories. Figure 2 presents the WCB trajectories and their
287 elevation during 48h. The ICE3 and LIMA trajectories and their ascending regions are very close
288 to each other but are not the same. For some trajectories ascends from the lower to the upper
289 troposphere occurs in localized regions of few degrees extent in longitude and latitude (see for

290 example 55°N, 32°W along the bent-back front) suggesting the possible occurrence of convective
291 motion as in Rasp et al. (2016) or Oertel et al. (2019) for instance.

292 Figure 3a shows different rising speeds between ICE3 and LIMA WCB trajectories. LIMA WCB
293 trajectories rise faster and slightly sooner than ICE3 WCB trajectories while having roughly the
294 same starting and ending heights. When looking at the latitudinal and longitudinal evolutions (not
295 shown), differences remain small suggesting that frontal risings are generally co-located in the two
296 runs.

297 Figure 3b shows the evolution of the five hydrometeor mass mixing ratios (ice, snow, graupel,
298 rain, droplets). For both runs, the warm hydrometeors undergo a sudden increase during the
299 first hour of the simulation while the cold hydrometeors are formed during the fifth hour. This
300 suggests that the spin-up of the model is less than 6 hours. Along these trajectories, the total
301 hydrometeor mixing content in ICE3 is twice as high as in LIMA, mainly due to ice, snow and
302 droplets contributions. These differences appear at the beginning of the simulations. In warm
303 hydrometeor category, droplets mass mixing ratios are larger in ICE3 than LIMA but the reverse
304 happens for rain mass mixing ratios. Consequently, highest hydrometeor contents along the WCB
305 are droplets then snow for ICE3 and rain then snow for LIMA.

306 Figure 3c presents the heating rate budgets of the two simulations and table 1 describes the
307 different processes contributing to those budgets. While the total mass mixing ratio differs strongly
308 between ICE3 and LIMA, the total heating rate does not exhibit large discrepancies between the
309 two runs. Slight differences are however noticeable. During the first 18 hours of the simulations,
310 LIMA exhibits slightly higher total heating rates than ICE3 while the reverse tends to happen later
311 during the second day of the simulations between 10 and 18 UTC 2 October. This is consistent with
312 the sooner ascends of the LIMA trajectories inside the WCB and the fact that the ICE3 trajectories
313 inside the WCB catch up the height of the LIMA trajectories during the second day (compare

314 Figs. 3a,c). While only slight differences are visible in the total heating rate, strong differences in
315 processes contributing to this total are noticeable. ICE3 heating is mainly due to deposition on ice
316 and droplets (DEPDI) while LIMA heating is due to deposition on ice and droplets (DEPDI), snow
317 (DEPS) and graupel (DEPG) by order of importance. There are many evidences that the relative
318 importance of the different heating rates cannot be directly linked to the different hydrometeor mass
319 mixing ratios. For instance, ICE3 exhibits greater snow mass mixing ratios than LIMA but the
320 heating rate due to depositional growth and sublimation of snow is slightly negative in ICE3 and
321 largely positive in LIMA. Hence, it mainly reflects sublimation of snow in ICE3 and results from
322 the fact that snow can only be formed via auto-conversion and aggregation of ice in ICE3 in cold
323 clouds. The graupel mass mixing ratios are almost the same in the two schemes while the heating
324 rate due to depositional growth and sublimation of graupel is positive in LIMA and near zero in
325 ICE3. Here again, this is due to the fact that graupel is not formed via such a process in ICE3 in
326 cold clouds. We also note that more cooling due to rain evaporation occurs in LIMA consistent
327 with higher values of rain mass mixing ratios. Finally, in both schemes, the fourth process of
328 importance is radiation. But because ICE3 exhibits a higher ice mass mixing ratio, the cooling due
329 to radiation is slightly more important in ICE3.

330 To conclude, despite producing similar total heating rates on average along the WCB trajectories,
331 the two simulations exhibit different heating budgets and the various processes contributing to
332 the total heating rate are quite different. Furthermore, we saw that ICE3 produces 30% more
333 WCB trajectories than LIMA. The following section is dedicated to more deeply investigate these
334 differences in WCB processes and their impact on the upper-tropospheric circulation.

335 **4. Impact on the ridge building**

336 Figures 4a and b represent the PV at the 315-K isentropic surface at 00 UTC 3 October for
337 ICE3 and LIMA respectively and the difference is shown in Fig. 4c. The 2 PVU limits used
338 to identify the dynamical tropopause (Appenzeller and Holton 1997; Grewe and Dameris 1996;
339 Blonsky and Speth 1998) are shown by dashed and solid green contours. Obviously, the most
340 important discrepancies occur in the area of large PV gradient values, that is, in the vicinity of the
341 tropopauses of the two simulations and in the stratosphere (left side of the 2 PVU limit). Two main
342 and opposite anomalies appear between ICE3 and LIMA near the tropopauses. The first one has a
343 narrow crescent shape spanning a large part of the ridge edge (61°N-76°N and 25°W-53°W). It is
344 hereafter called the red PV anomaly and corresponds to a 3° northwestward shift of the tropopause
345 with ICE3 compared to LIMA. The second one is more localized and located to the south of the
346 ridge (59.5°N-62.5°N and 31°W-42°W). It is hereafter called the blue PV anomaly and corresponds
347 to a ~2° southward shift of the tropopause with LIMA compared to ICE3. The differences in PV in
348 those regions between LIMA and ICE3 are of the same order of magnitude as those found by Joos
349 and Forbes (2016) while comparing two microphysics schemes used in IFS. The red PV anomaly
350 forms from the beginning of the simulations at the leading edge of the ridge building while the
351 blue PV anomaly begins to form 36 hours later above the cold front and slightly north of it in
352 convective regions as shown later. The two anomalies reflect spatial shifts of the tropopause region
353 and changes in the PV gradient that has some consequences on the wind speed as discussed later
354 in section 5.

355 As expected, WCB trajectories are mainly inside the ridge. The red and blue WCB trajectories
356 are defined as WCB trajectories being in the troposphere and belonging to the red and blue PV
357 anomalies respectively in areas where the anomalies go beyond 1 PVU. After computation of the

358 curvature of the WCB trajectories (or the relative vorticity along them) we found that the red
359 and blue PV anomalies correspond to anticyclonic and cyclonic trajectories respectively. Because
360 they correspond to cyclonic trajectories forming above the cold front, blue WCB trajectories bring
361 similarities with the WCB trajectories studied by Oertel et al. (2019) and Blanchard et al. (2020)
362 that have fast convective ascends. This aspect will be confirmed later. Consistent with the negative
363 sign of the PV anomalies and because more WCB trajectories mean more diabatically produced
364 negative PV, ICE3 gets more WCB trajectories (723) inside the red PV anomaly than LIMA (260),
365 while LIMA gets more WCB trajectories (101) reaching the blue PV anomaly than ICE3 (42).

366 *a. Anomaly at the leading edge of the ridge building*

367 This subsection is dedicated to studying the formation of the red PV anomaly appearing along
368 the leading edge of the ridge building. Figures 5a, b and c show the vertically averaged total
369 heating rate between 2 km and 9 km at 18 UTC 2 October for ICE3, LIMA and their difference
370 respectively. The large values of heating rate cover broader regions along the cold and bent-back
371 warm fronts with ICE3 than LIMA. Figures 5e-f show vertical cross sections of the meridionally
372 averaged heating rate where most of the WCB trajectories ending up in the red PV anomaly (purple
373 points) are located, that is along a significant part of the warm front (see the dark box in Figs. 5a-c).
374 At this time, most of the trajectories are near the tropopause above the large values of heating rate
375 and tend to complete their ascent, and some of them are still in the upper side of the strong heating
376 area. On these cross sections, we also see that the strong heating area is larger in ICE3 and the
377 peak values of the heating rate are 50% higher in ICE3 than LIMA (about 1.5 K h^{-1} for ICE3
378 and 1.0 K h^{-1} for LIMA). Above 2 km, that is mainly above the melting layer, the most important
379 processes contributing to the heating rate are deposition on ice with ICE3 and deposition on snow
380 and graupel for LIMA (Figs. 5d-e). Below 2 km, condensational growth of droplets dominates

381 for both schemes. In agreement with the PV tendency equation, stronger diabatic heating leads
382 to stronger vertical gradient aloft and stronger PV destruction in ICE3 than in LIMA. We also
383 checked that the divergent winds are more intense in the former run than in the latter, leading
384 to more intense PV advection which amplifies more rapidly the ridge in ICE3. The differential
385 heating (~ 0.5 K at maximum) between ICE3 and LIMA likely explains the 1° tropopause shift
386 between ICE3 and LIMA (Fig. 5f) via its direct effect (PV destruction) and its indirect effect
387 (PV advection by divergent winds).

388 Figure 6 shows the temporal evolution of height and potential temperature tendencies associated
389 with the main microphysical processes (deposition on droplets and ice, on snow and on graupel)
390 for the WCB trajectories corresponding to the red PV anomaly. As expected, rapid ascends co-
391 occur with intense heating rates in both runs (Figs. 6a,c). However, the timing of the largest total
392 heating rates strongly differs between ICE3 and LIMA. Between 12 UTC 1 October and 00 UTC 2
393 October, the heating is slightly stronger in LIMA due to strong condensational growth of droplets
394 as mass mixing ratios indicate the presence of droplets and not ice at that time (not shown). As
395 a consequence, the WCB ascends faster in LIMA during that period. During the next 6 hours,
396 between 00 UTC and 06 UTC 2 October, the two total heating rates are roughly equivalent and the
397 WCB trajectories exhibit the same order of elevation in the two runs (Figs. 6a,c). Between 06 UTC
398 2 October and 00 UTC 3 October, the heating is stronger for ICE3 due to stronger depositional
399 growth of ice which is not compensated by the stronger heating due to deposition on graupel and
400 snow for LIMA (Figs. 6c-f).

401 Figure 6b shows the number of trajectories that have already ascended 600 hPa since the initial
402 time starting at zero by construction. The first trajectories ascending 600 hPa appear at 18 UTC
403 1 October. While the averaged heating along those WCB trajectories is initially stronger for
404 LIMA, the number of trajectories satisfying 600 hPa ascends never exceeds that for ICE3 (Fig. 6b).

405 However, we do see that the difference in the number of trajectories accentuates robustly after 06
406 UTC 2 October due to stronger depositional growth of ice in ICE3 (Figs. 6c-d).

407 To conclude, the ICE3 WCB trajectories reaching the red PV anomaly are more numerous than
408 the LIMA WCB trajectories arriving in that region because the heating is stronger and spans larger
409 areas in ICE3 to the north of the cyclone. This does not mean that the heating averaged along the
410 selected WCB trajectories is stronger in ICE3. But the processes leading to the heating largely
411 differ. Adjustment to saturation on ice performed in ICE3 and not in LIMA (explicit deposition)
412 may explain the more important vapor deposition on ice in ICE3, its stronger heating in average at
413 upper levels and the more numerous WCB trajectories found for that scheme. This picture of the
414 WCB trajectories finishing their trajectories in the red PV anomaly reflects the difference between
415 the WCB trajectories of ICE3 and LIMA in general. However, in some areas, the situation might
416 be different as discussed in next subsection.

417 *b. Anomaly in the cyclonic branch of the WCB*

418 WCB trajectories contributing to the formation of the blue PV anomaly shown in Fig. 4 are
419 mainly located above the cold front on its northern part at 18 UTC 2 October (Figs. 5a,b). To
420 better visualize the heating rates and WCB trajectories in that region, a zoom is made in Fig.7. The
421 formation of the blue PV anomaly is already seen by the more southwestward shift of the tropopause
422 in LIMA compared to ICE3 (see solid and dashed green contours). This region is characterized
423 by less homogeneous heating rates than further south along the cold front and is more marked by
424 isolated patches of heating rate suggesting the presence of embedded convection on the northern
425 edge of the cold front similarly to Oertel et al. (2020) or Blanchard et al. (2020) (see e.g., at 29
426 °W and 59.5°N for both runs). ascends of these WCB trajectories are fast for the ensemble of the
427 trajectories (600 hPa in ~ 12 hours) and some individual ascends are even faster, confirming the

428 presence of convection. By zonally averaging the heating rate on 21-31°W, it clearly appears that
429 the localized heating rate near 60°N is much stronger in LIMA with the peak values being above
430 1.5 K h⁻¹ for LIMA and slightly less than 1.0 K h⁻¹ for ICE3. As for the other WCB trajectories,
431 the heating in the ice phase is mainly due to vapor deposition on ice for ICE3 and vapor deposition
432 on snow and graupel for LIMA (see Figs. 7d-e). However, in that particular case, the depositional
433 growth of snow and graupel in LIMA is larger than the depositional growth of ice in ICE3 in
434 contrast with many other regions and in particular the red PV anomaly discussed earlier. In Fig. 7,
435 the negative PV anomaly and the shift between the two tropopauses being just above the heating rate
436 anomaly, it suggests that the vertical gradient of the heating is important to create the PV anomaly
437 and not necessarily the horizontal gradient as in Oertel et al. (2020) or Blanchard et al. (2021).
438 The interpretation of the formation of the negative PV anomaly is confirmed by the presence of
439 more numerous WCB trajectories in LIMA than ICE3 between 59°N and 61°N above 6 km. As the
440 divergent wind is northward in both runs in the vicinity of this anomaly, and not oriented towards
441 the stratospheric reservoir it suggests that there is no reinforcement of this anomaly by the indirect
442 effect of PV advection by the divergent winds (not shown). This is to be contrasted with the case
443 of the red anomaly for which the divergent winds participate in reinforcement of the anomaly.

444 To sum up, the blue PV anomaly seems to be a consequence of discrepancies between the two
445 simulations in the activity of isolated convective cells on the northern leading edge of the cold
446 front. Since the two runs largely differ in the vicinity of the tropopauses, next section is dedicated
447 to identify which run performs better when compared to the observations.

448 **5. Comparison between model simulations and observations**

449 Figure 8 shows the PV and the wind differences between LIMA and ICE3 roughly at the time of
450 the flights: at 10 UTC for flight F6 that last from ~ 9:00 to ~ 11:30 (Figs. 8a,c) and at 16 UTC for

451 flight F7 that last from $\sim 13:00$ to $\sim 16:00$ (Figs. 8b,d). Flight F6 intersects the red PV anomaly
452 in the morning (Fig. 8a). The PV gradient differences associated with the PV anomaly along the
453 tropopause are responsible of a dipolar wind anomaly with larger negative than positive values (see
454 blue and red shaded areas in Fig. 8c on both sides of the tropopauses). This creates a broader and
455 more northwestward shifted jet stream in ICE3 than LIMA. Flight F7 is in the vicinity of the blue
456 PV anomaly when it starts to be formed (Fig. 8b). This creates higher wind speed values in the
457 southwestern corner of the flight for LIMA than ICE3 (Fig. 8d). Since flights F6 and F7 crossed
458 the red and blue PV anomalies respectively, airborne measurements are well suited to evaluate the
459 skills of the two simulations.

460 *a. Satellite*

461 Before comparing with dropsondes and RALI retrieved data, a comparison of the brightness
462 temperatures at $10.8 \mu\text{m}$ as simulated by ICE3 and LIMA with the observed one from the Meteosat
463 Second Generation (MSG) satellite (Schmetz et al. 2002) is made in Fig. 9. To estimate the cloud
464 brightness temperature at $10.8 \mu\text{m}$ as viewed by a satellite, the RTTOV (Radiative Transfer for
465 TOVS) version 11.3 fast radiative transfer model is used (Saunders et al. 2013). The comparison
466 is made at 12 UTC 2 October, as it is the closest intermediate time between the two flights for
467 which we have satellite data. The dark and light blue shadings indicate the presence of high and
468 mid-to-low clouds respectively while the dark red represents the Sea Surface Temperature. Three
469 main regions of high clouds can be detected from the satellite product in Fig.9c: a band near
470 19°W - 13°W extending from 44°N to 60°N and corresponding to the high clouds associated with
471 the cold front, the WCB outflow region where flight F6 was located and another region between
472 37°W - 31°W and 54°N - 60°N near the bent-back warm front. The red part on the southwestern
473 corner of flight F7 situates the dry intrusion.

474 The most obvious difference between the model and the observations is that the cloud top is
475 warmer in the simulations. This discrepancy is more pronounced with LIMA, which possibly
476 means that LIMA does not simulate clouds as high as ICE3 does. Otherwise, the ICE3 and LIMA
477 simulations seem to correctly represent the position of the fronts and WCB.

478 *b. Dropsondes*

479 The wind speed profiles observed by the dropsondes launched during F6, in particular the four
480 westernmost dropsondes labelled as '095544', '100414', '102617', and '103200', allow us to assess
481 the skills of the two simulations in representing the location of the tropopause and the upper-level
482 winds (Fig. 10). These dropsondes are particularly well suited to compare the skills of the LIMA
483 and ICE3 simulations as they are located within the red PV anomaly (Fig. 8a). At upper levels,
484 between 8 and 10 km, the two dropsondes '095544' and '103200' exhibit observed wind speed
485 values near 45 m s^{-1} which are rather well represented by the two simulations. The two others,
486 namely '100414' and '102617', located to the extreme west of the flight show observed values
487 near 30 m s^{-1} . For those two dropsondes, strong discrepancies appear between LIMA and ICE3
488 simulations; LIMA underestimates the observed values between 8 and 10 km while ICE3 is much
489 closer to the observations at those heights. This is particularly cogent in Fig. 10c. This corresponds
490 to the negative wind anomalies shown in Fig. 8c and associated with the red PV anomaly of Fig. 8a.
491 Our conclusion is that ICE3 better represents the upper-level wind speeds in the region of the red
492 PV anomaly, and that the position of the tropopause in ICE3 is more realistic than in LIMA.

493 *c. Remote sensing measurements*

494 Figure 11 shows the wind and reflectivity as measured by the radar below the aircraft and as
495 simulated by ICE3 and LIMA along flight F7. The aircraft flew along the central triangle shown in

496 Fig. 9 by following a clockwise path. Since the radar is only sensitive to hydrometeors, observations
497 are only available in cloudy and precipitating areas. Even though the jet stream is crossed twice
498 only the wind speed values on its northern flank are measured by the radar and the blank values
499 between 15:00 and 15:30 correspond to the flank of the jet stream within the dry intrusion. In-situ
500 airborne measurements of wind speed correlate fairly well with the radar measurements (Fig. 11a).
501 Wind patterns are correctly represented by ICE3 and LIMA in regions where radar observations
502 exist.

503 In LIMA, the jet is stronger and narrower than in ICE3 as already shown in Fig. 8d in relation
504 with the blue PV anomaly. The spatial extension of the jet stream is slightly better represented
505 with ICE3 (see in-situ data at 15:45) and the peak values of the jet stream are also more consistent
506 with observed ones in ICE3 (between 15:10 and 15:30). This is confirmed by the root mean square
507 values along the flight which are lower with ICE3 (1.9 m.s^{-1}) than LIMA (3.0 m.s^{-1}).

508 Figure 11b compares the observed and simulated reflectivities. There is no observed reflectivity
509 above 8 km because the aircraft flew at this altitude and the radar was only pointing downward.
510 Many features of the observed reflectivity are found in the simulated reflectivity like the strong
511 reflectivity near 1430 UTC and 1545 UTC corresponding to deep cloudy structures along the
512 WCB. The dry area in between these two regions is also represented. Another common feature
513 between the simulations and the observations is the altitude of the melting layer located near 2 km.
514 However, very important discrepancies appear and the skills of the simulations strongly depend on
515 the altitude.

516 Below the melting layer, the reflectivity values are rather well reproduced by the model (see
517 Figs. 11d-f and Figs. 12a-c). This is particularly true for LIMA (see the pdfs Figs. 12a-c). Root
518 mean squared errors are indeed only 1.6 dBZ for LIMA and 2.8 dBZ for ICE3.

519 Above the melting layer, in the middle troposphere between 2 km and 6 km, the reflectivity
520 values are largely underestimated in the simulations compared to the observations, about 5 dBz
521 for ICE3 and about 10 dBz for LIMA. At this altitude, snow and graupel predominate. This might
522 be due to the fact that snow mass-concentration distribution disagrees with observations as shown
523 in Taufour et al. (2018). Besides, the current radar simulator uses the Mie scattering rather than
524 other complex method, such as the T-matrix and this may suffer from rather large errors in the solid
525 phase and may underestimate the reflectivity (e.g., Hogan et al. 2012; Borderies et al. 2018).

526 In the upper troposphere, between 6 km and 8 km, ICE3 reflectivity is higher than LIMA
527 reflectivity and is close to the observed reflectivity: ICE3 reflectivity varies between -5 dB and -15
528 dB on average as in the observations while LIMA reflectivity is below -20 dB at those heights (see
529 black curves in Figs. 12a-c). At altitudes higher than 8 km, where there is no observed reflectivity
530 for that flight, LIMA still simulates much weaker reflectivity than ICE3. This suggests that fewer
531 hydrometeors are present in LIMA at high altitude. It is consistent with Fig. 9 where cloud top
532 temperatures are found to be warmer and likely lower in altitude with LIMA than ICE3.

533 When considering the variations with height of the reflectivity, LIMA presents the closest shape
534 to the observations as both LIMA and the observed reflectivity values decrease with height from
535 3 km and 8 km while ICE3 reflectivity values do not present such a decrease. More precise
536 vertical distribution with LIMA could be due to a more accurate cold species distribution and
537 vapor depositional growth. Indeed, LIMA uses an explicit vapor deposition on snow, graupel and
538 ice, while ICE3 uses one supersaturation distribution for ice and another one for graupel and snow
539 in mixed-phase clouds. When a vertical integration is made, LIMA reflectivity is also slightly
540 greater than ICE3 but this results from the warm phase below the melting layer (Fig. 12d). As
541 previously said, ICE3 has higher reflectivity than LIMA in cold phase and in that sense is closer to
542 the observations.

543 Model-to-radar and radar-to-model approaches are complementary to address the weaknesses
544 associated with the assumptions inherent to both approaches. Figures 12e-h compare PDFs of
545 Ice Water Content (IWC). As with the reflectivity, we only consider IWC values that can be
546 retrieved with RALI in our comparison. A log scale is also used to get closer to the reflectivity
547 variable which is shown in decibels. Above 6 km, ICE3 is close to the observations and clearly
548 exhibits greater values than LIMA: ICE3 ice water content fluctuates between 0.03 and 0.1 gm^{-3}
549 roughly like the retrieved ice water content while LIMA ice water content values are much lower
550 between 0.01 and 0.05 gm^{-3} . Below 6 km height, LIMA and ICE3 strongly underestimate the
551 quantities of cold species compared to the observations but LIMA produces a more realistic
552 vertical distribution. The main conclusions concerning the reflectivity PDFs are thus confirmed
553 when looking at the IWC PDFs. Therefore the main differences between the simulations and
554 the observations are unlikely to be attributed to the way the reflectivity is calculated in the
555 models or the way IWC is retrieved. These underestimation could be attributed to microphysical
556 misrepresentations like the hydrometeors fall speed or mass-diameter distribution. Also, ver-
557 tically integrated water content could be lower than reality due to misrepresented air-sea exchanges.

558
559 To sum up, Meso-NH reproduces the observed wind very well. However, the two simulations
560 clearly underestimate the IWC and reflectivity above the melting layer. LIMA produces the closest
561 variations with altitude but ICE3 is better in intensity. As previously hypothesized, adjustment
562 to saturation in cold and mixed phases realized only by ICE3, may explain why ICE3 produces
563 more cold hydrometeors but prognostic vapor deposition on parallel on ice, snow and graupel with
564 LIMA may explain the better vertical profile of cold hydrometeor contents.

565 **6. Conclusion and discussion**

566 The present study is part of a joint international effort under the banner of the NAWDEX field
567 campaign to better assess the skills of NWP models in representing subgrid-scale diabatic processes
568 within mid-latitude cyclones. It more precisely investigates the impact of two cloud microphysical
569 schemes developed within the mesoscale Meso-NH model on the development of an extratropical
570 cyclone during IOP 6, called the Stalactite Cyclone, its associated warm conveyor belt, and the ridge
571 building aloft. Two 72-hour simulations with a 2.5-km resolution are performed and compared:
572 one with the one-moment scheme ICE3 and the second one with the quasi two-moment scheme
573 LIMA. ICE3 and LIMA also differ on the processes of vapor deposition on hydrometeors in cold
574 and mixed-phase clouds.

575 The first part of the study was dedicated to presenting differences in WCB trajectories, hy-
576 drometeor mixing ratios and heating rates along the WCB and how these differences impact the
577 upper-level ridge building in the WCB outflow region. The following results were found:

- 578 • Strong heating rate covers larger areas along the cold and bent-back warm front in ICE3 than
579 LIMA. This explains why WCB trajectories in ICE3 are 33% more numerous than in LIMA
580 even though the averaged total heating rates along them are equivalent. In comparison, Joos
581 and Forbes (2016) found the same number of WCB trajectories by running their model with
582 two distinct microphysical schemes.
- 583 • Despite having roughly the same heating rate along WCB trajectories, the hydrometeor con-
584 tents and the processes participating in the heating budget along WCB trajectories largely
585 differ from one run to another. Latent heating in ICE3 is dominated by deposition on ice while
586 the heating in LIMA is distributed among depositions on ice, snow and graupel.

- 587 • The timing of the WCB ascends also differ between the two runs. While WCB ascends of
588 LIMA occur in a rather small time window, those of ICE3 are more spread out during the run.
- 589 • The stronger WCB activity in ICE3 provides an explanation for the generally more rapid ridge
590 building in ICE3 than LIMA, which is more obvious in the anticyclonic branch of the WCB
591 outflow. In the cyclonic branch, the reverse happens in a rather localized region where the
592 tropopause is more rapidly pushed outward in LIMA. This is due to more active fast ascends
593 within localized convective cells north of the cold front resembling those studied by Oertel
594 et al. (2019, 2020) and Blanchard et al. (2020, 2021).

595 The second part of the results was dedicated to the comparison with satellite observations and
596 airborne observations collected during two flights of the SAFIRE Falcon-20 on 2 October 2016.

597 The main results are:

- 598 • The wind speed measured by the dropsondes during flight F6 at the leading edge of the ridge
599 building resembles more that simulated by ICE3 than LIMA. Closer to the cyclone center,
600 in-situ airborne measurements and radar Doppler measurements of flight F7 also support
601 the idea that ICE3 performs slightly better than LIMA in the representation of upper-level
602 circulation.
- 603 • A comparison of the simulated brightness temperatures with the observed one from MSG
604 shows that the cooler (or higher altitude) clouds found in ICE3 than LIMA are more realistic.
- 605 • The comparison between the simulated reflectivities computed with the radar forward operator
606 of Borderies et al. (2018) and the observed reflectivity shows that (i) above 6 km, the ICE3
607 reflectivity is higher than the LIMA one and closer to the observations, (ii) between 2 km
608 and 6 km, both ICE3 and LIMA reflectivities largely underestimate the observed one and (iii)
609 below the melting layer, the observed reflectivity is slightly better represented by LIMA. When

610 looking at the vertical distribution LIMA is more realistic but it more largely underestimates
611 the observed reflectivity in the cold phase than ICE3.

- 612 • The comparison between the retrieved IWC computed with the DARDAR-CLOUD algorithm
613 (Delanoë and Hogan 2008) and the model IWC confirms the reflectivity results. Above 6 km,
614 the ICE3 IWC is higher and closer to the retrieved IWC than to LIMA IWC. Between 2 km
615 and 6 km, both simulations largely underestimate IWC by an average factor of 2 to 3 but the
616 underestimation is more pronounced in LIMA. This result is consistent with the hydrometeors
617 mass mixing ratio underestimation along the WCB with LIMA compared to ICE3.

618 Both the radar-to-model and model-to-radar approaches provide the same picture giving us con-
619 fidence in the results: the cold hydrometeors are largely underestimated by the model and more
620 importantly by LIMA.

621 The present study relies on the representation of an unique extratropical cyclone, which was a
622 very deep cyclone triggered by synoptic-scale upper-level forcing and characterized by a very active
623 warm conveyor belt. Dearden et al. (2016) stated that a strong dynamical forcing could overshadow
624 microphysical sensitivities. This is the reason why similar simulations have been performed for a
625 more moderate extratropical cyclone observed during IOP 10 of NAWDEX (Schäfler et al. 2018;
626 Sánchez et al. 2020; Steinfeld et al. 2020) that had a weaker synoptic forcing. This case, which is
627 referred to as the Thor ridge case in Schäfler et al. (2018), led to more numerous WCB trajectories
628 in ICE3 than LIMA (55% more) that lead to a more rapidly amplified ridge building with ICE3
629 (not shown). Other sensitivity experiments have been made by changing the starting times of the
630 simulations of the two cyclones and by using ECMWF datasets to initialize and force the model
631 and this did not change the main picture provided in the present study. While the intensity of the

632 PV anomaly may depend on the starting times and the domain extension, the previously mentioned
633 tests provide confidence in the general character of our comparison between LIMA and ICE3.

634 The comparisons with observations emphasize the important issue of the large underestimation
635 of the reflectivity and ice water content in the model. It has also been observed in all our sensitivity
636 tests. Such an underestimation has also been noticed by Rysman et al. (2018) over the Mediterranean
637 comparing the Weather and Research Forecasting model to satellite and radar data over a two-year
638 period. They pointed out the need of providing more realistic frozen hydrometeor contents.

639 Our hypothesis is that it is the adjustment to saturation in cold and mixed phases that helps ICE3
640 to get more ice than LIMA. This leads to a better representation of the WCB and more accurate
641 upper-level dynamics in the former than the latter run even though the adjustment to saturation
642 has less physical meaning than an explicit vapor deposition. This importance of the adjustment to
643 saturation is supported by some sensitivity tests that we have performed. In particular, as LIMA
644 does not have a subgrid condensation scheme, we turned it off in ICE3 and this change had rather
645 small effects in IWC, reflectivity and upper-level ridge even though non negligible. Two approaches
646 can be envisaged in the future to get the model more realistic:

- 647 • In ICE3 and LIMA, one possibility will be to improve the representation of hydrometeors,
648 especially by modifying the snow particle size distribution assumptions. In LIMA another
649 possibility will be to test a new version including a two-moment description of snow and
650 graupel. Impact of such changes should be on snow and graupel fall speeds and mass mixing
651 ratios.
- 652 • In ICE3, different ways of determining the supersaturation distribution between liquid and
653 solid will be tested in mixed-phase cloud. Such choices might have an impact on latent heating
654 release in middle troposphere as latent release is stronger for vapor to ice than vapor to liquid.

655 For operational purposes, it is important to more systematically compare ICE3 and LIMA to better
656 characterize in which situations one scheme performs better than the other. Taufour et al. (2018)
657 underlined the better behavior of LIMA in the representation of two convective precipitation events
658 during HyMeX while the present study rather shows the reverse in a large-scale extratropical
659 cyclone. More case studies would be needed to confirm these preliminary results.

660 **Acknowledgements**

661 We thank David Flack for proofreading an early version of the manuscript and correcting the
662 English spelling and grammar. This work was funded by several projects: EARTHCARE RALI
663 NAWDEX - EPATAN ESA Contract No. 4000119015/NL|CT/gp, CNES AEOLUS/EECLAT,
664 F-NAWDEX of the French national programme INSU/LEFE and ANR DIP-NAWDEX (ANR-17-
665 CE01-0010).

666 **Data Availability Statement**

667 Data available on request from the authors.

References

- Appenzeller, C., and J. R. Holton, 1997: Tracer lamination in the stratosphere: A global climatology. *Journal of Geophysical Research: Atmospheres*, **102 (D12)**, 13 555–13 569.
- Augros, C., O. Caumont, V. Ducrocq, N. Gaussiat, and P. Tabary, 2016: Comparisons between S-, C- and X-band polarimetric radar observations and convective-scale simulations of the hymex first special observing period. *Quarterly Journal of the Royal Meteorological Society*, **142**, 347–362.
- Avramov, A., and J. Y. Harrington, 2010: Influence of parameterized ice habit on simulated mixed phase arctic clouds. *Journal of Geophysical Research: Atmospheres*, **115 (D3)**.
- Berman, J. D., and R. D. Torn, 2019: The impact of initial condition and warm conveyor belt forecast uncertainty on variability in the downstream waveguide in an ecwmf case study. *Monthly Weather Review*, **147 (11)**, 4071–4089.
- Binder, H., M. Boettcher, H. Joos, and H. Wernli, 2016: The role of warm conveyor belts for the intensification of extratropical cyclones in Northern Hemisphere winter. *Journal of the Atmospheric Sciences*, **73 (10)**, 3997–4020.
- Blanchard, N., F. Pantillon, J.-P. Chaboureau, and J. Delanoë, 2020: Organization of convective ascents in a warm conveyor belt. *Weather and Climate Dynamics*, **1 (2)**, 617–634.
- Blanchard, N., F. Pantillon, J.-P. Chaboureau, and J. Delanoë, 2021: Mid-level convection in a warm conveyor belt accelerates the jet stream. *Weather and Climate Dynamics*, **2**, 37–53.
- Blonsky, S., and P. Speth, 1998: An algorithm to detect tropopause folds from ozone soundings. *Meteorologische Zeitschrift*, 153–162.

689 Borderies, M., and Coauthors, 2018: Simulation of W-band radar reflectivity for model validation
690 and data assimilation. *Quarterly Journal of the Royal Meteorological Society*, **144** (711), 391–
691 403.

692 Bougeault, P., and P. Lacarrere, 1989: Parameterization of orography-induced turbulence in a
693 mesobeta-scale model. *Monthly Weather Review*, **117** (8), 1872–1890.

694 Brogniez, G., C. Pietras, M. Legrand, P. Dubuisson, and M. Haeffelin, 2003: A high-accuracy
695 multiwavelength radiometer for in situ measurements in the thermal infrared. part ii: Behavior
696 in field experiments. *Journal of Atmospheric and Oceanic Technology*, **20** (7), 1023–1033.

697 Browning, K. A., 1986: Conceptual models of precipitation systems. *Weather and Forecasting*,
698 **1** (1), 23–41.

699 Caniaux, G., J. Redelsperger, and J. P. Lafore, 1994: A numerical study of the stratiform region of
700 a fast-moving squall line. part I: General description and water and heat budgets. *Journal of the*
701 *atmospheric sciences*, **51** (14), 2046–2074.

702 Caumont, O., and Coauthors, 2006: A radar simulator for high-resolution nonhydrostatic models.
703 *Journal of Atmospheric and Oceanic Technology*, **23** (8), 1049–1067.

704 Cazenave, Q., 2019: Development and evaluation of multisensor methods for EarthCare mission
705 based on A-Train and airborne measurements. Theses, Université Paris-Saclay, URL <https://tel.archives-ouvertes.fr/tel-02076316>.
706

707 Chaboureau, J.-P., and P. Bechtold, 2002: A simple cloud parameterization derived from cloud
708 resolving model data: Diagnostic and prognostic applications. *J. Atmos. Sci.*, **59**, 2362–2372,
709 doi:10.1175/1520-0469(2002)059<2362:ASCPDF>2.0.CO;2, URL [http://dx.doi.org/10.1175/
710 1520-0469\(2002\)059<2362:ASCPDF>2.0.CO;2](http://dx.doi.org/10.1175/1520-0469(2002)059<2362:ASCPDF>2.0.CO;2).

711 Cohard, J.-M., J.-P. Pinty, and C. Bedos, 1998: Extending Twomey’s analytical estimate of
712 nucleated cloud droplet concentrations from CCN spectra. *Journal of the atmospheric sciences*,
713 **55 (22)**, 3348–3357.

714 Colella, P., and P. R. Woodward, 1984: The piecewise parabolic method (ppm) for gas-dynamical
715 simulations. *Journal of computational physics*, **54 (1)**, 174–201.

716 Coronel, B., D. Ricard, G. Rivière, and P. Arbogast, 2015: Role of moist processes in the tracks of
717 idealized midlatitude surface cyclones. *Journal of the Atmospheric Sciences*, **72 (8)**, 2979–2996.

718 Crezee, B., H. Joos, and H. Wernli, 2017: The microphysical building blocks of low-level potential
719 vorticity anomalies in an idealized extratropical cyclone. *Journal of the Atmospheric Sciences*,
720 **74 (5)**, 1403–1416.

721 Cuxart, J., P. Bougeault, and J.-L. Redelsperger, 2000: A turbulence scheme allowing for mesoscale
722 and large-eddy simulations. *Quarterly Journal of the Royal Meteorological Society*, **126 (562)**,
723 1–30.

724 Davis, C. A., M. T. Stoelinga, and Y.-H. Kuo, 1993: The integrated effect of condensation in
725 numerical simulations of extratropical cyclogenesis. *Monthly weather review*, **121 (8)**, 2309–
726 2330.

727 Dearden, C., G. Vaughan, T. Tsai, and J.-P. Chen, 2016: Exploring the diabatic role of ice
728 microphysical processes in two North Atlantic summer cyclones. *Monthly Weather Review*,
729 **144 (4)**, 1249–1272.

730 Delanoë, J., and R. J. Hogan, 2008: A variational scheme for retrieving ice cloud properties from
731 combined radar, lidar, and infrared radiometer. *Journal of Geophysical Research: Atmospheres*,
732 **113 (D7)**.

733 Delanoë, J., A. Protat, O. Jourdan, J. Pelon, M. Papazzoni, R. Dupuy, J.-F. Gayet, and C. Jouan,
734 2013: Comparison of airborne in situ, airborne radar–lidar, and spaceborne radar–lidar retrievals
735 of polar ice cloud properties sampled during the polarcat campaign. *Journal of Atmospheric and*
736 *Oceanic Technology*, **30** (1), 57–73.

737 Dirren, S., M. Didone, and H. Davies, 2003: Diagnosis of “forecast-analysis” differences of a
738 weather prediction system. *Geophysical research letters*, **30** (20).

739 Ducrocq, V., and Coauthors, 2014: Hymex-sop1: The field campaign dedicated to heavy precipi-
740 tation and flash flooding in the northwestern mediterranean. *Bulletin of the American Meteoro-*
741 *logical Society*, **95** (7), 1083–1100.

742 Eckhardt, S., A. Stohl, H. Wernli, P. James, C. Forster, and N. Spichtinger, 2004: A 15-year
743 climatology of warm conveyor belts. *Journal of climate*, **17** (1), 218–237.

744 Flack, D., G. Rivière, I. Musat, R. Roehrig, S. Bony, J. Delanoë, Q. Cazenave, and J. Pelon,
745 2021: Representation by two climate models of the dynamical and diabatic processes involved
746 in the development of an explosively-deepening cyclone during nawdex. *Weather and Climate*
747 *Dynamics*, **2**, in press.

748 Forbes, R. M., and P. A. Clark, 2003: Sensitivity of extratropical cyclone mesoscale structure to the
749 parametrization of ice microphysical processes. *Quarterly Journal of the Royal Meteorological*
750 *Society: A journal of the atmospheric sciences, applied meteorology and physical oceanography*,
751 **129** (589), 1123–1148.

752 Gehring, J., A. Oertel, É. Vignon, N. Jullien, N. Besic, and A. Berne, 2020: Microphysics and
753 dynamics of snowfall associated with a warm conveyor belt over korea. *Atmospheric Chemistry*
754 *and Physics*, **20** (12), 7373–7392.

- 755 Gettelman, A., and Coauthors, 2010: Global simulations of ice nucleation and ice supersaturation
756 with an improved cloud scheme in the community atmosphere model. *Journal of Geophysical*
757 *Research: Atmospheres*, **115 (D18)**.
- 758 Gheusi, F., and J. Stein, 2002: Lagrangian description of airflows using Eulerian passive tracers.
759 *Quarterly Journal of the Royal Meteorological Society: A journal of the atmospheric sciences,*
760 *applied meteorology and physical oceanography*, **128 (579)**, 337–360.
- 761 Gierens, K. M., M. Monier, and J.-F. Gayet, 2003: The deposition coefficient and its role for cirrus
762 clouds. *Journal of Geophysical Research: Atmospheres*, **108 (D2)**.
- 763 Gray, S. L., C. Dunning, J. Methven, G. Masato, and J. M. Chagnon, 2014: Systematic model
764 forecast error in rossby wave structure. *Geophysical Research Letters*, **41 (8)**, 2979–2987.
- 765 Grewe, V., and M. Dameris, 1996: Calculating the global mass exchange between stratosphere and
766 troposphere. *Annales Geophysicae*, Springer, Vol. 14, 431–442.
- 767 Harrold, T., 1973: Mechanisms influencing the distribution of precipitation within baroclinic
768 disturbances. *Quarterly Journal of the Royal Meteorological Society*, **99 (420)**, 232–251.
- 769 Hashimoto, A., M. Murakami, T. Kato, and M. Nakamura, 2007: Evaluation of the influence of
770 saturation adjustment with respect to ice on meso-scale model simulations for the case of 22
771 june, 2002. *SOLA*, **3**, 85–88.
- 772 Heymsfield, A. J., L. M. Miloshevich, C. Twohy, G. Sachse, and S. Oltmans, 1998: Upper-
773 tropospheric relative humidity observations and implications for cirrus ice nucleation. *Geophys-*
774 *ical research letters*, **25 (9)**, 1343–1346.

775 Hogan, R. J., L. Tian, P. R. Brown, C. D. Westbrook, A. J. Heymsfield, and J. D. Eastment,
776 2012: Radar scattering from ice aggregates using the horizontally aligned oblate spheroid
777 approximation. *Journal of Applied Meteorology and Climatology*, **51 (3)**, 655–671.

778 Holton, J., 2004: An introduction to dynamic meteorology, int. *Geophys. Ser.*, **88**, 313–369.

779 Hoskins, B. J., M. McIntyre, and A. W. Robertson, 1985: On the use and significance of isentropic
780 potential vorticity maps. *Quarterly Journal of the Royal Meteorological Society*, **111 (470)**,
781 877–946.

782 Joos, H., and R. M. Forbes, 2016: Impact of different IFS microphysics on a warm conveyor
783 belt and the downstream flow evolution. *Quarterly Journal of the Royal Meteorological Society*,
784 **142 (700)**, 2727–2739.

785 Joos, H., and H. Wernli, 2012: Influence of microphysical processes on the potential vorticity
786 development in a warm conveyor belt: A case-study with the limited-area model COSMO.
787 *Quarterly Journal of the Royal Meteorological Society*, **138 (663)**, 407–418.

788 Kessler, E., 1969: On the distribution and continuity of water substance in atmospheric circulations.
789 *On the distribution and continuity of water substance in atmospheric circulations*, Springer, 1–
790 84.

791 Khain, A., and Coauthors, 2015: Representation of microphysical processes in cloud-resolving
792 models: Spectral (bin) microphysics versus bulk parameterization. *Reviews of Geophysics*,
793 **53 (2)**, 247–322.

794 Kuo, Y.-H., M. Shapiro, and E. G. Donall, 1991: The interaction between baroclinic and diabatic
795 processes in a numerical simulation of a rapidly intensifying extratropical marine cyclone.
796 *Monthly Weather Review*, **119 (2)**, 368–384.

797 Lac, C., and Coauthors, 2018: Overview of the Meso-NH model version 5.4 and its applications.
798 *Geoscientific Model Development*, **11**, 1929–1969.

799 Maddison, J., S. Gray, O. Martinez-Alvarado, and K. Williams, 2019: Upstream cyclone influence
800 on the predictability of block onsets over the Euro-Atlantic region. *Monthly Weather Review*,
801 **147**, 1277–1296.

802 Madonna, E., H. Wernli, H. Joos, and O. Martius, 2014: Warm conveyor belts in the ERA-Interim
803 dataset (1979–2010). part i: Climatology and potential vorticity evolution. *Journal of climate*,
804 **27** (1), 3–26.

805 Manabe, S., 1956: On the contribution of heat released by condensation to the change in pressure
806 pattern. *Journal of the Meteorological Society of Japan. Ser. II*, **34** (6), 308–320.

807 Martínez-Alvarado, O., E. Madonna, S. L. Gray, and H. Joos, 2016: A route to systematic error in
808 forecasts of Rossby waves. *Quarterly Journal of the Royal Meteorological Society*, **142** (694),
809 196–210.

810 Meyers, M. P., P. J. DeMott, and W. R. Cotton, 1992: New primary ice-nucleation parameterizations
811 in an explicit cloud model. *Journal of Applied Meteorology*, **31** (7), 708–721.

812 Mishchenko, M. I., L. D. Travis, and D. W. Mackowski, 1996: T-matrix computations of light scat-
813 tering by nonspherical particles: A review. *Journal of Quantitative Spectroscopy and Radiative*
814 *Transfer*, **55** (5), 535–575.

815 Mlawer, E. J., S. J. Taubman, P. D. Brown, M. J. Iacono, and S. A. Clough, 1997: Radiative transfer
816 for inhomogeneous atmospheres: RRTM, a validated correlated-k model for the longwave.
817 *Journal of Geophysical Research: Atmospheres*, **102** (D14), 16 663–16 682.

- 818 Morcrette, J.-J., 1991: Radiation and cloud radiative properties in the European Centre for Medium
819 Range Weather Forecasts forecasting system. *Journal of Geophysical Research: Atmospheres*,
820 **96 (D5)**, 9121–9132.
- 821 Oertel, A., M. Boettcher, H. Joos, M. Sprenger, H. Konow, M. Hagen, and H. Wernli, 2019: Con-
822 vective activity in an extratropical cyclone and its warm conveyor belt—a case-study combining
823 observations and a convection-permitting model simulation. *Quarterly Journal of the Royal
824 Meteorological Society*.
- 825 Oertel, A., M. Sprenger, H. Joos, M. Boettcher, H. Konow, M. Hagen, and H. Wernli, 2020:
826 Observations and simulation of intense convection embedded in a warm conveyor belt—how
827 ambient vertical wind shear determines the dynamical impact. *Weather and Climate Dynamics
828 Discussions*, 1–35.
- 829 Pergaud, J., V. Masson, S. Malardel, and F. Couvreur, 2009: A parameterization of dry thermals
830 and shallow cumuli for mesoscale numerical weather prediction. *Boundary-layer meteorology*,
831 **132 (1)**, 83.
- 832 Phillips, V. T., P. J. DeMott, and C. Andronache, 2008: An empirical parameterization of het-
833 erogeneous ice nucleation for multiple chemical species of aerosol. *Journal of the atmospheric
834 sciences*, **65 (9)**, 2757–2783.
- 835 Phillips, V. T., P. J. Demott, C. Andronache, K. A. Pratt, K. A. Prather, R. Subramanian, and
836 C. Twohy, 2013: Improvements to an empirical parameterization of heterogeneous ice nucleation
837 and its comparison with observations. *Journal of the Atmospheric Sciences*, **70 (2)**, 378–409.
- 838 Pinty, J., and P. Jabouille, 1998: A mixed-phase cloud parameterization for use in mesoscale
839 non-hydrostatic model: simulations of a squall line and of orographic precipitations. *Conf. on*

- 840 *Cloud Physics*, American Meteorological Society Everett, WA, 217–220.
- 841 Pomroy, H. R., and A. J. Thorpe, 2000: The evolution and dynamical role of reduced upper-
842 tropospheric potential vorticity in intensive observing period one of FASTEX. *Monthly Weather*
843 *Review*, **128 (6)**, 1817–1834.
- 844 Rasp, S., T. Selz, and G. C. Craig, 2016: Convective and slantwise trajectory ascent in convection-
845 permitting simulations of midlatitude cyclones. *Monthly Weather Review*, **144 (10)**, 3961–3976.
- 846 Reisin, T., Z. Levin, and S. Tzivion, 1996: Rain production in convective clouds as simulated in
847 an axisymmetric model with detailed microphysics. part i: Description of the model. *Journal of*
848 *the atmospheric sciences*, **53 (3)**, 497–519.
- 849 Robertson, F., and P. Smith, 1983: The impact of model moist processes on the energetics of
850 extratropical cyclones. *Monthly Weather Review*, **111 (4)**, 723–744.
- 851 Rossa, A., H. Wernli, and H. Davies, 2000: Growth and decay of an extra-tropical cyclone’s
852 pv-tower. *Meteorology and Atmospheric Physics*, **73 (3)**, 139–156.
- 853 Rysman, J.-F., S. Berthou, C. Claud, P. Drobinski, J.-P. Chaboureau, and J. Delanoë, 2018: Potential
854 of microwave observations for the evaluation of rainfall and convection in a regional climate
855 model in the frame of hymex and med-cordex. *Climate dynamics*, **51 (3)**, 837–855.
- 856 Sánchez, C., J. Methven, S. Gray, and M. Cullen, 2020: Linking rapid forecast error growth to
857 diabatic processes. *Quarterly Journal of the Royal Meteorological Society*, **146 (732)**, 3548–
858 3569.
- 859 Saunders, R., and Coauthors, 2013: RTTOV-11 science and validation report, NWP/SAF technical
860 document n. Tech. rep., NWPSAF-MO-TV-032.

- 861 Schäfler, A., and Coauthors, 2018: The North Atlantic Waveguide and Downstream impact
862 EXperiment. *Bulletin of the American Meteorological Society*, **99** (8), 1607–1637.
- 863 Schmetz, J., P. Pili, S. Tjemkes, D. Just, J. Kerkmann, S. Rota, and A. Ratier, 2002: An introduction
864 to Meteosat Second Generation (MSG). *Bulletin of the American Meteorological Society*, **83** (7),
865 977–992.
- 866 Seity, Y., P. Brousseau, S. Malardel, G. Hello, P. Bénard, F. Bouttier, C. Lac, and V. Masson, 2011:
867 The AROME-France convective-scale operational model. *Monthly Weather Review*, **139** (3),
868 976–991.
- 869 Steinfeld, D., M. Boettcher, R. Forbes, and S. Pfahl, 2020: The sensitivity of atmospheric blocking
870 to changes in upstream latent heating—numerical experiments. *Weather and Climate Dynamics*
871 *Discussions*, 1–32.
- 872 Taufour, M., and Coauthors, 2018: Evaluation of the two-moment scheme LIMA based on micro-
873 physical observations from the HyMeX campaign. *Quarterly Journal of the Royal Meteorological*
874 *Society*, **144** (714), 1398–1414.
- 875 Tompkins, A. M., K. Gierens, and G. Rädcl, 2007: Ice supersaturation in the ecmwf integrated fore-
876 cast system. *Quarterly Journal of the Royal Meteorological Society: A journal of the atmospheric*
877 *sciences, applied meteorology and physical oceanography*, **133** (622), 53–63.
- 878 Vié, B., J.-P. Pinty, S. Berthet, and M. Leriche, 2016: LIMA (v1. 0): A quasi two-moment
879 microphysical scheme driven by a multimodal population of cloud condensation and ice freezing
880 nuclei. *Geoscientific Model Development*, **9** (2), 567–586.

881 Wernli, B. H., and H. C. Davies, 1997: A Lagrangian-based analysis of extratropical cyclones.
882 I: The method and some applications. *Quarterly Journal of the Royal Meteorological Society*,
883 **123 (538)**, 467–489.

884 **List of Tables**

885 **Table 1.** Abbreviation of the main processes participating in the heating rate budget of
886 the simulations. 44

Abbreviation	Description of process
DEPDI	Depositional growth of droplets and ice
DEPS	Depositional growth of snow/sublimation of snow (ICE3, growth only in mixed phase)
DEPG	Depositional growth of graupel/sublimation of graupel (ICE3, growth only in mixed phase)
RAD	Radiative heating/cooling rate
GMLT	Graupel melting
REVA	Rain evaporation

Table 1. Abbreviation of the main processes participating in the heating rate budget of the simulations.

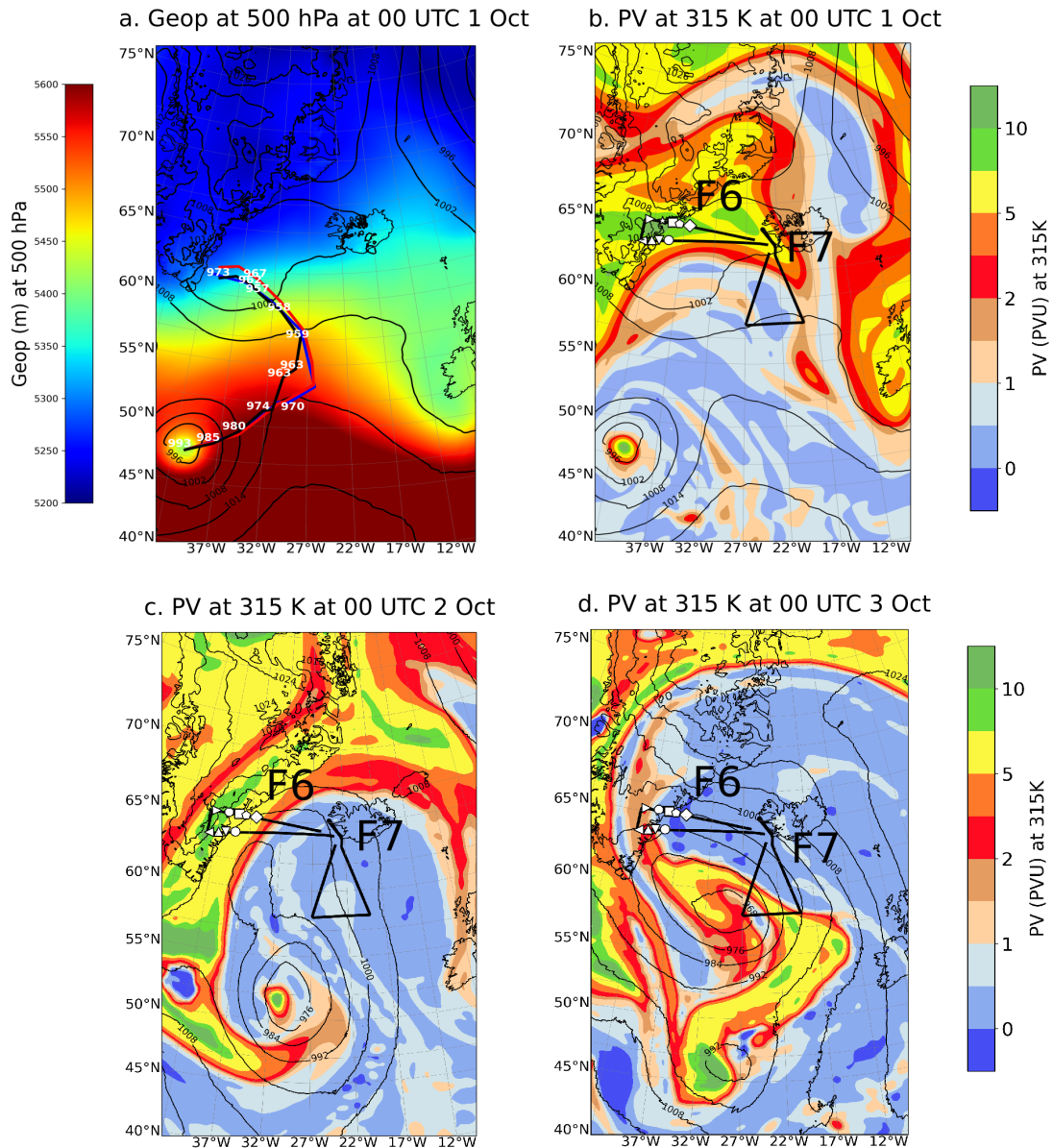
887 List of Figures

- 888 **Fig. 1.** (a) Geopotential height at 500 hPa from ARPEGE operational analysis at 00 UTC 1 Oct. The black, blue
889 and red lines represent the 6-hourly evolution from 00 UTC 1 Oct to 00 UTC 4 Oct of the Sea Level Pressure
890 (SLP) minimum for ARPEGE analysis, ICE3 run and LIMA run respectively. (b)-(d) PV at the 315-K
891 isentropic surface (shading; units: PVU) and SLP (black contours; int: 8 hPa) for ICE3 run at (b) 00 UTC
892 1 Oct, (c) 00 UTC 2 Oct and (d) 00 UTC 3 Oct. The flight tracks F6 and F7 are shown by the bold lines in
893 b-d. Symbols indicate the launch location for each dropsondes during flight F6. 47
- 894 **Fig. 2.** WCB trajectories colored according to altitude for (left) ICE3 and (right) LIMA. Seeding has been performed
895 in the whole domain every 8 grid points along the horizontal directions at 00 UTC 3 Oct. One over twenty
896 trajectories are plotted for visibility sake. 48
- 897 **Fig. 3.** (a) Time evolution of the altitude of the WCB trajectories between 00 UTC 1 Oct and 00 UTC 3 Oct. Light
898 shadings represent the 5th and 95th percentiles and dark shadings the 25th and 75th percentiles, the full
899 lines the median and the dashed lines the mean. Time evolution of (b) the hydrometeor mass mixing ratios
900 and (c) the heating rates of the main processes averaged over ICE3 (solid lines) and LIMA (dashed lines)
901 trajectories. Abbreviations are given in table 1. 49
- 902 **Fig. 4.** PV at the 315-K isentropic surface for (a) ICE3, (b) LIMA and (c) the difference LIMA-ICE3 at 00 UTC 3
903 Oct. The 2 PVU isoline is represented by a green full and dashed line for ICE3 and LIMA respectively. In
904 (a),(b), WCB trajectories intersecting the isentrope $315\text{ K} \pm 5\text{ K}$ at the plot time are shown in black dots.
905 Purple and cyan dots represent the WCB trajectories corresponding to the red (r) and blue (b) PV anomalies
906 shown along the tropopause in (c) (see text for more details on the definition of the anomalies). Only one
907 WCB over 5 are represented for visibility sake. 50
- 908 **Fig. 5.** (Upper panels) Vertically averaged heating rate between 2 km and 9 km (shadings) and (lower panels)
909 meridionally averaged heating rate (shadings) in the larger black area shown in upper panels at 18 UTC 2
910 Oct for (a),(d) ICE3, (b),(e) LIMA and (c),(f) the difference LIMA-ICE3. Black dots in (a),(b) correspond
911 to WCB trajectories positions at 18 UTC 2 Oct, while the purple and blue dots to the trajectories ending
912 in the red and blue PV anomalies respectively shown in Fig. 4c. In the upper panels one WCB over 5 are
913 represented for visibility sake. Green lines represents the position of the dynamic tropopause (full line in
914 ICE3 and dashed line in LIMA). The grey and black lines in (f) represent the 1 PVU and 0.5 PVU difference
915 between LIMA and ICE3 (solid lines for positive and dashed for negative). The purple, blue and orange
916 lines in (e),(f) represent the DEPDI, DEPS, and DEPG contributions respectively when it is greater than 0.3 K.h^{-1}
917 (solid for positive and dashed for negative). 51
- 918 **Fig. 6.** Time evolution between 00 UTC 1 Oct and 00 UTC 3 Oct along the computed WCB trajectories reaching
919 the red PV anomaly of (a) altitude, (c) the total heating rates, (d) the heating rate due to deposition of vapor
920 on droplets or ice, (e) the heating rate due to the deposition of vapor on snow and (f) the heating rate due to
921 the deposition on graupel. Light shadings represent the 5th and 95th percentiles and dark shadings the 25th
922 and 75th percentiles, the full lines the median and the dashed ones the mean. (b) Number of trajectories
923 reaching the red PV anomaly at 00 UTC 3 Oct and having ascended 600 hPa between the initial time and a
924 given time (blue for ICE3 and red for LIMA). 52
- 925 **Fig. 7.** (a)-(c) same as Figs. 5(a)-(c) but in the zoomed area centred on the small black box. (d)-(f) zonally averaged
926 heating rate (shadings) in the black area shown in upper panels for (a),(d) ICE3, (b),(e) LIMA and (c),(f)
927 the difference LIMA-ICE3. Color, dots and lines legends are the same as in Fig. 5. 53
- 928 **Fig. 8.** (a),(b) PV and (c),(d) wind difference LIMA-ICE3 at the 315-K isentropic surface at (a),(c) 10 UTC 2 Oct
929 and (b),(d) 16 UTC on 2 Oct. F6 flight track (from $\sim 9:00$ to $\sim 11:30$) is represented by the top-left triangle.
930 F7 flight track (from $\sim 13:00$ to $\sim 16:00$) is represented by the bottom triangle. 54
- 931 **Fig. 9.** Brightness temperature at $10.8\ \mu\text{m}$ at 12 UTC 2 Oct 2016 for the (a) ICE3, (b) LIMA and (C) the MSG
932 observation. The black lines represent the two flight tracks. 55

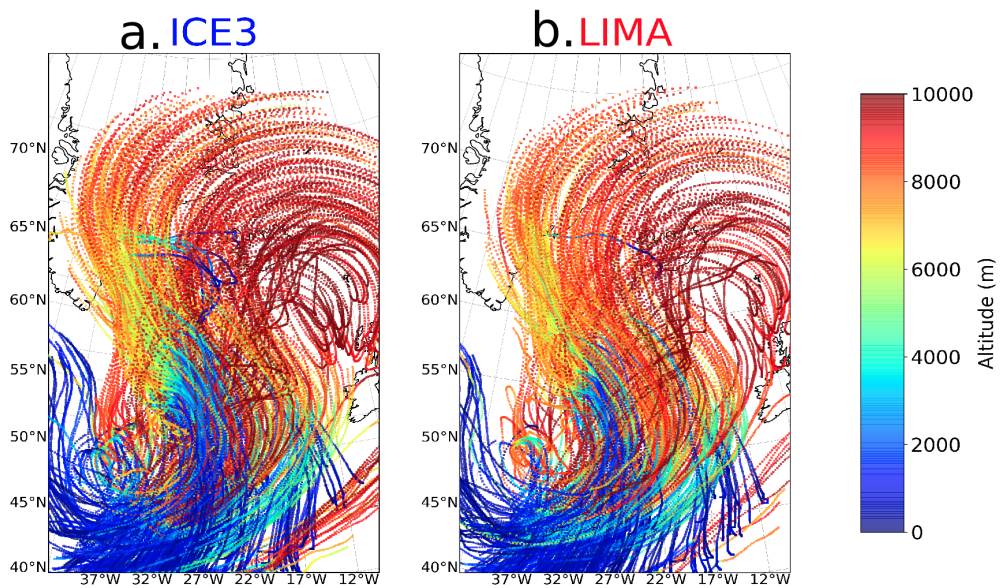
933 **Fig. 10.** Wind speed as observed (in black) from the 4 westernmost dropsondes launched during F6 over Greenland
934 coast (see symbols in Figs. 4 or 9 indicating the launch location for each dropsonde) and simulated with
935 ICE3 (in blue) and LIMA (in red). Each dropsonde is labelled according to the launch time using the format
936 hhmmss. 56

937 **Fig. 11.** (a)-(c) Horizontal wind speed and (d)-(f) reflectivity along flight F7 (see bottom triangle in Fig. 9) for (upper
938 panels) RASTA observations, (middle panels) ICE3 simulation, and (lower panels) LIMA simulation. The
939 vertical dark lines stand for the time where the flight changed direction. Wind speed as measured by the
940 in-situ aircraft instrument at the flight level are added on (a)-(c) with the same color bar. The RASTA data
941 are regridded onto the Meso-NH grid. 57

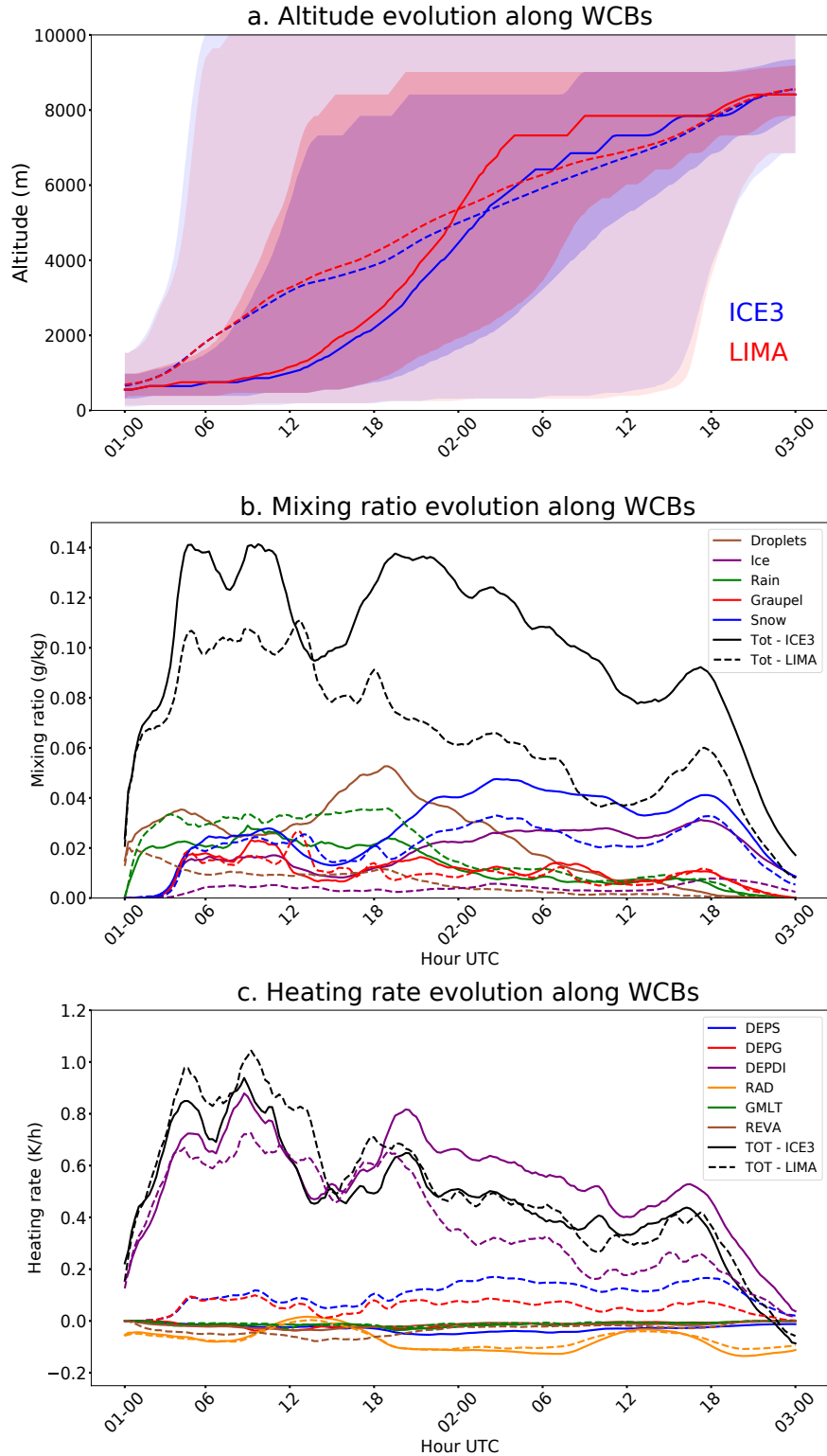
942 **Fig. 12.** Bivariate PDFs as a function of altitude of (a)-(c) reflectivity and (e)-(g) Ice Water Content for (a),(e)
943 ICE3, (b),(f) LIMA and (c),(g) the observations regridded onto the model grid, mean vertical profiles are
944 indicated for ICE3 (dotted line), LIMA (dashed line), and observations (solid line). The measurements and
945 observations are normalized with the total number of points. Panels (d) and (h) correspond to the sum over
946 height of the bivariate PDFs of reflectivity and IWC respectively with ICE3 (in blue), LIMA (in red) and
947 observations (in black). 58



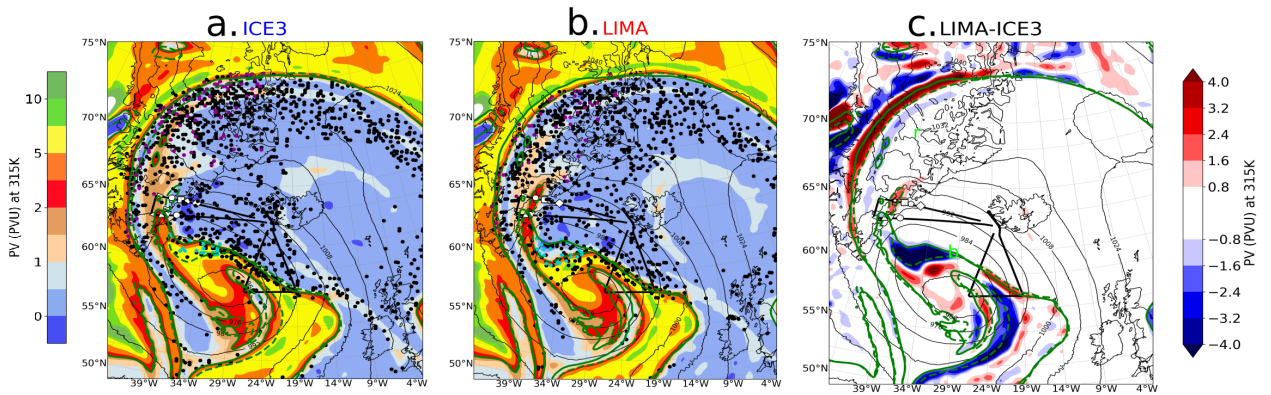
948 Figure 1. (a) Geopotential height at 500 hPa from ARPEGE operational analysis at 00 UTC 1 Oct. The black, blue and red
 949 lines represent the 6-hourly evolution from 00 UTC 1 Oct to 00 UTC 4 Oct of the Sea Level Pressure (SLP) minimum for ARPEGE
 950 analysis, ICE3 run and LIMA run respectively. (b)-(d) PV at the 315-K isentropic surface (shading; units: PVU) and SLP (black
 951 contours; int: 8 hPa) for ICE3 run at (b) 00 UTC 1 Oct, (c) 00 UTC 2 Oct and (d) 00 UTC 3 Oct. The flight tracks F6 and F7
 952 are shown by the bold lines in b-d. Symbols indicate the launch location for each dropsondes during flight F6.



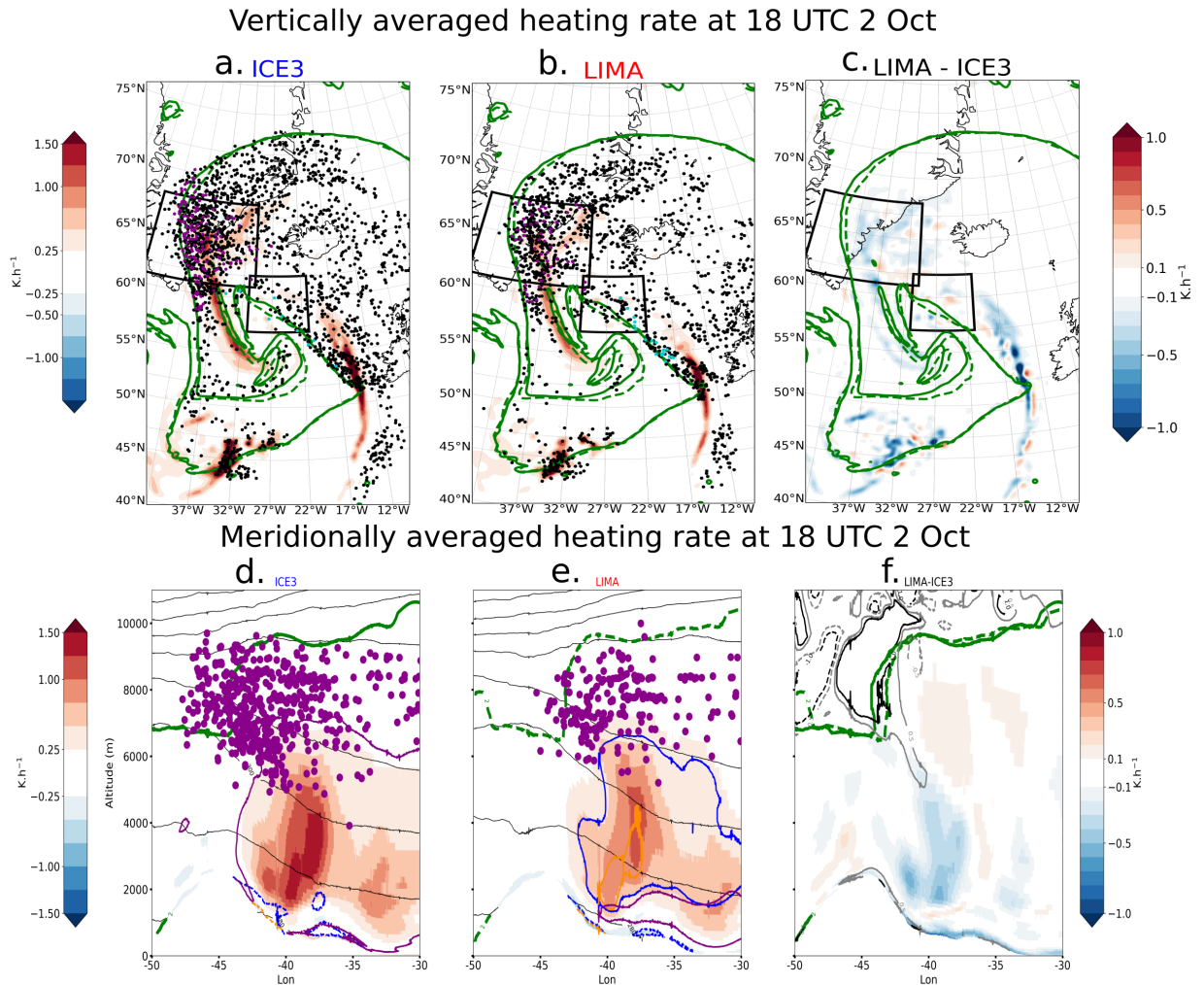
953 Figure 2. WCB trajectories colored according to altitude for (left) ICE3 and (right) LIMA. Seeding has been performed in the
 954 whole domain every 8 grid points along the horizontal directions at 00 UTC 3 Oct. One over twenty trajectories are plotted for
 955 visibility sake.



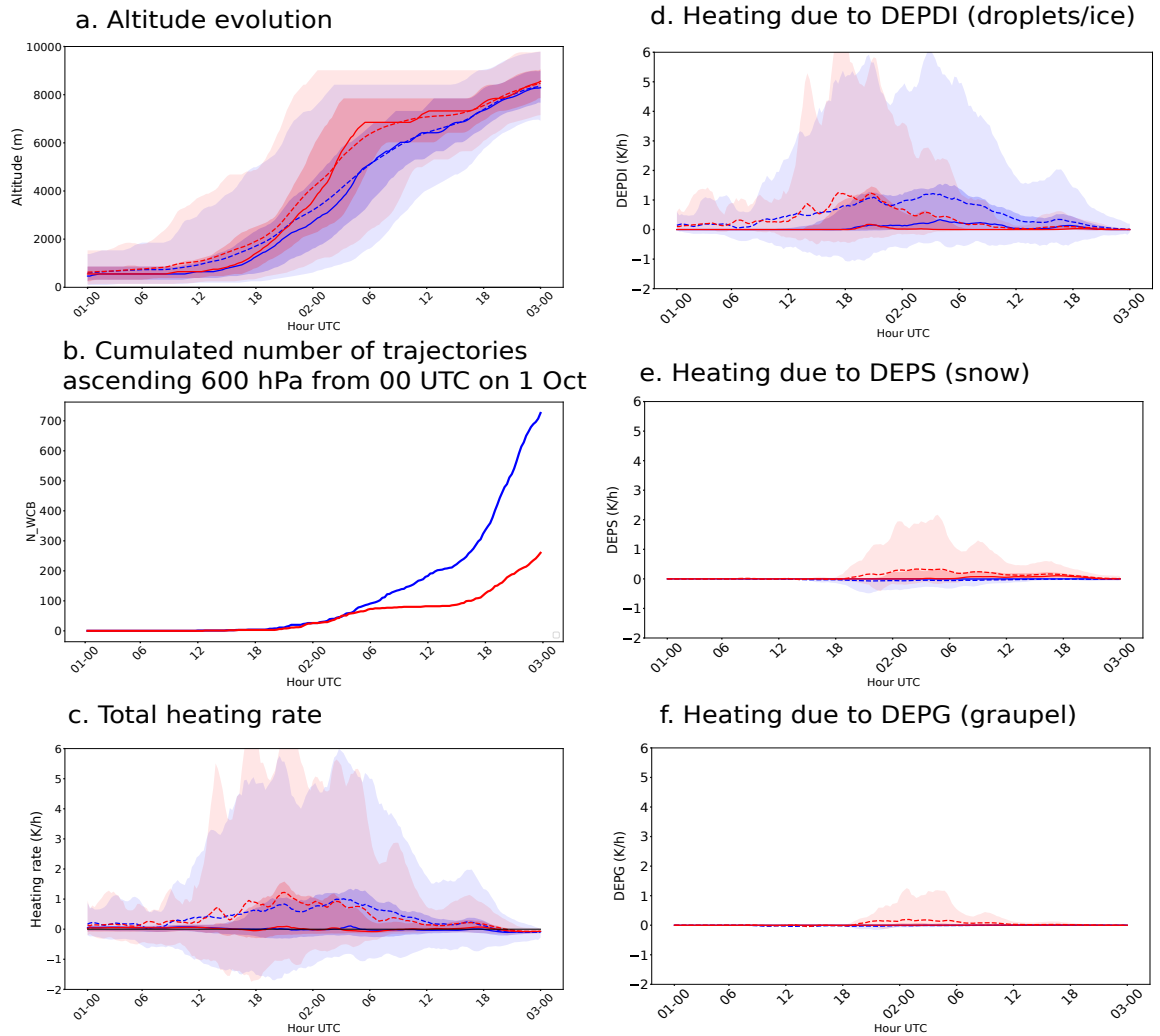
956 **Figure 3.** (a) Time evolution of the altitude of the WCB trajectories between 00 UTC 1 Oct and 00 UTC 3 Oct. Light shadings
 957 represent the 5th and 95th percentiles and dark shadings the 25th and 75th percentiles, the full lines the median and the dashed
 958 lines the mean. Time evolution of (b) the hydrometeor mass mixing ratios and (c) the heating rates of the main processes averaged
 959 over ICE3 (solid lines) and LIMA (dashed lines) trajectories. Abbreviations are given in table 1.



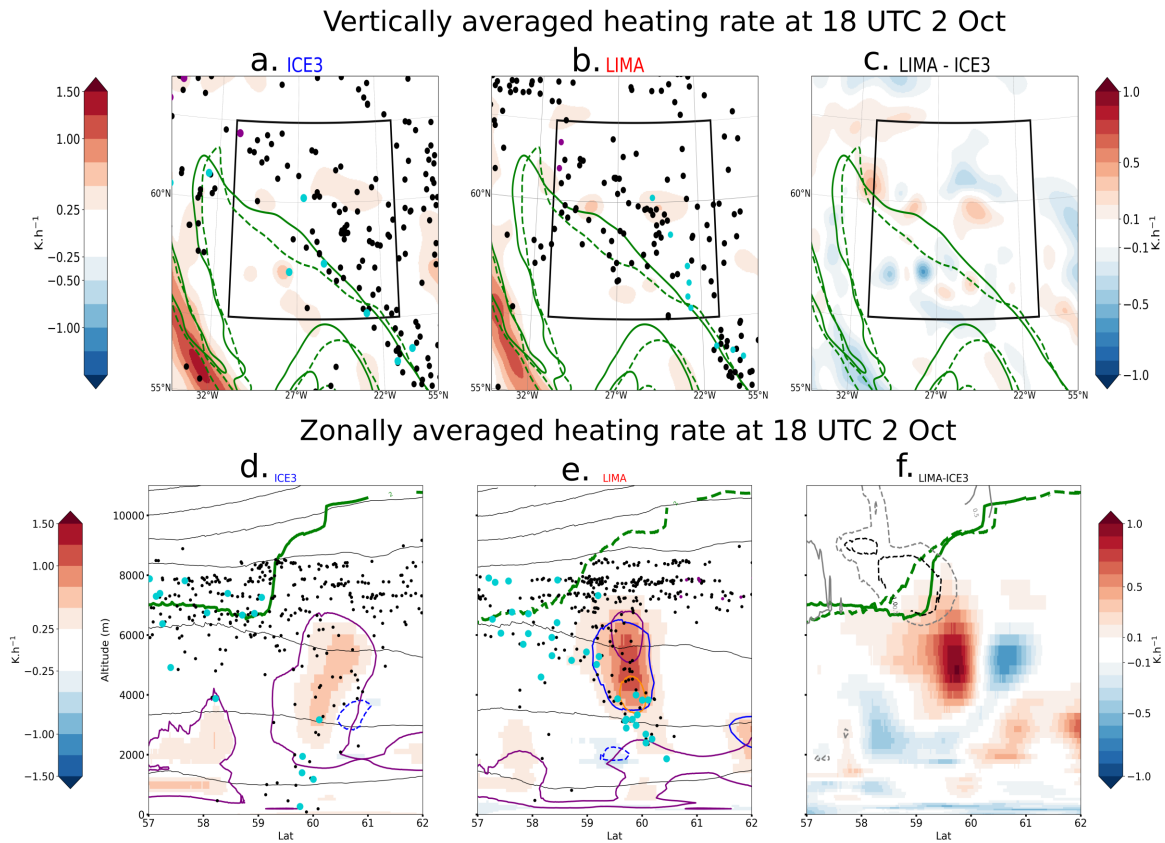
960 Figure 4. PV at the 315-K isentropic surface for (a) ICE3, (b) LIMA and (c) the difference LIMA-ICE3 at 00 UTC 3 Oct.
 961 The 2 PVU isoline is represented by a green full and dashed line for ICE3 and LIMA respectively. In (a),(b), WCB trajectories
 962 intersecting the isentropes $315 \text{ K} \pm 5 \text{ K}$ at the plot time are shown in black dots. Purple and cyan dots represent the WCB trajectories
 963 corresponding to the red (r) and blue (b) PV anomalies shown along the tropopause in (c) (see text for more details on the definition
 964 of the anomalies). Only one WCB over 5 are represented for visibility sake.



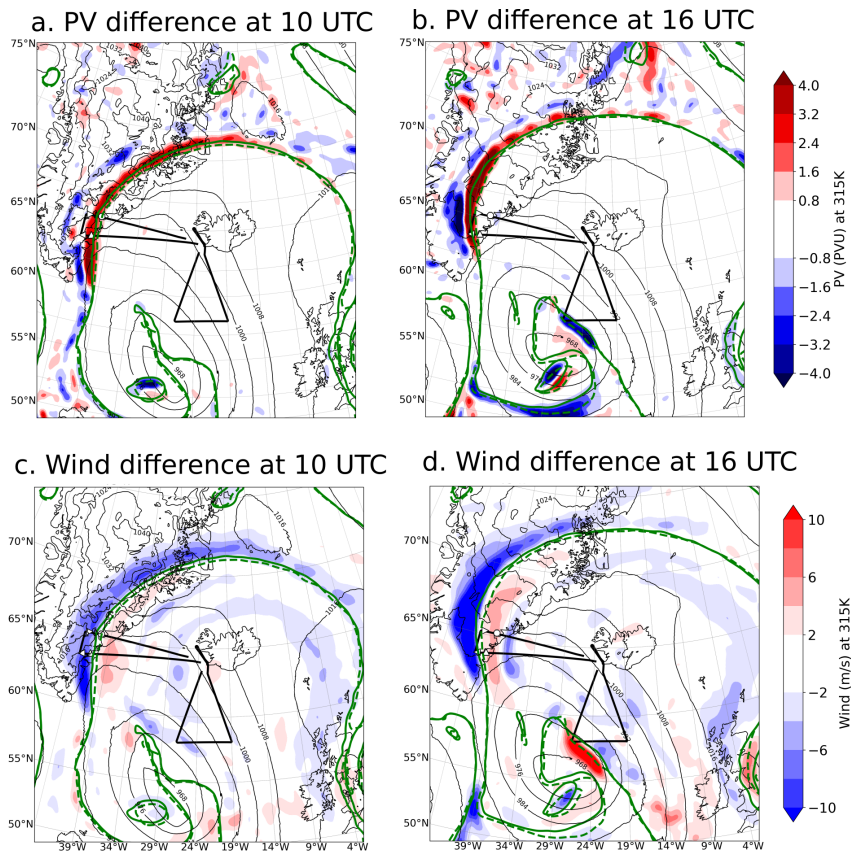
965 **Figure 5.** (Upper panels) Vertically averaged heating rate between 2 km and 9 km (shadings) and (lower panels) meridionally
 966 averaged heating rate (shadings) in the larger black area shown in upper panels at 18 UTC 2 Oct for (a),(d) ICE3, (b),(e) LIMA
 967 and (c),(f) the difference LIMA-ICE3. Black dots in (a),(b) correspond to WCB trajectories positions at 18 UTC 2 Oct, while the
 968 purple and blue dots to the trajectories ending in the red and blue PV anomalies respectively shown in Fig. 4c. In the upper panels
 969 one WCB over 5 are represented for visibility sake. Green lines represents the position of the dynamic tropopause (full line in ICE3
 970 and dashed line in LIMA). The grey and black lines in (f) represent the 1 PVU and 0.5 PVU difference between LIMA and ICE3
 971 (solid lines for positive and dashed for negative). The purple, blue and orange lines in (e),(f) represent the DEPDI, DEPS, and
 972 DEPG contributions respectively when it is greater than 0.3 K.h^{-1} (solid for positive and dashed for negative).



973 **Figure 6.** Time evolution between 00 UTC 1 Oct and 00 UTC 3 Oct along the computed WCB trajectories reaching the red PV
 974 anomaly of (a) altitude, (c) the total heating rates, (d) the heating rate due to deposition of vapor on droplets or ice, (e) the heating
 975 rate due to the deposition of vapor on snow and (f) the heating rate due to the deposition on graupel. Light shadings represent the
 976 5th and 95th percentiles and dark shadings the 25th and 75th percentiles, the full lines the median and the dashed ones the mean.
 977 (b) Number of trajectories reaching the red PV anomaly at 00 UTC 3 Oct and having ascended 600 hPa between the initial time and
 978 a given time (blue for ICE3 and red for LIMA).



979 Figure 7. (a)-(c) same as Figs. 5(a)-(c) but in the zoomed area centred on the small black box. (d)-(f) zonally averaged heating
 980 rate (shadings) in the black area shown in upper panels for (a),(d) ICE3, (b),(e) LIMA and (c),(f) the difference LIMA-ICE3. Color,
 981 dots and lines legends are the same as in Fig. 5.



982 Figure 8. (a),(b) PV and (c),(d) wind difference LIMA-ICE3 at the 315-K isentropic surface at (a),(c) 10 UTC 2 Oct and (b),(d)
 983 16 UTC on 2 Oct. F6 flight track (from ~ 9:00 to ~ 11:30) is represented by the top-left triangle. F7 flight track (from ~ 13:00 to
 984 ~ 16:00) is represented by the bottom triangle.

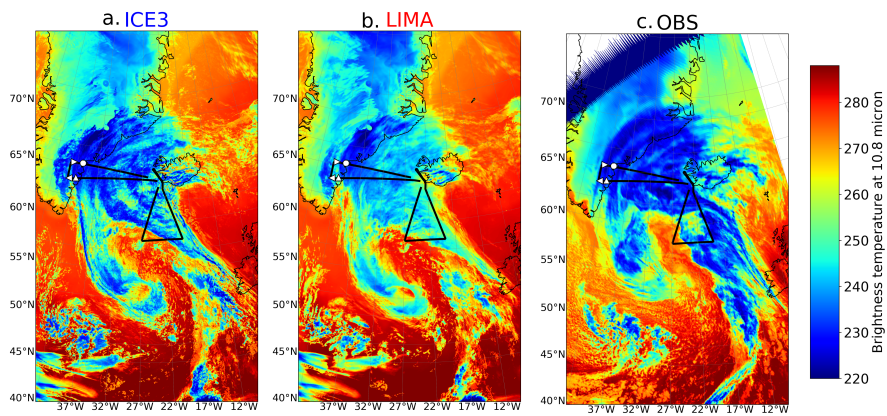
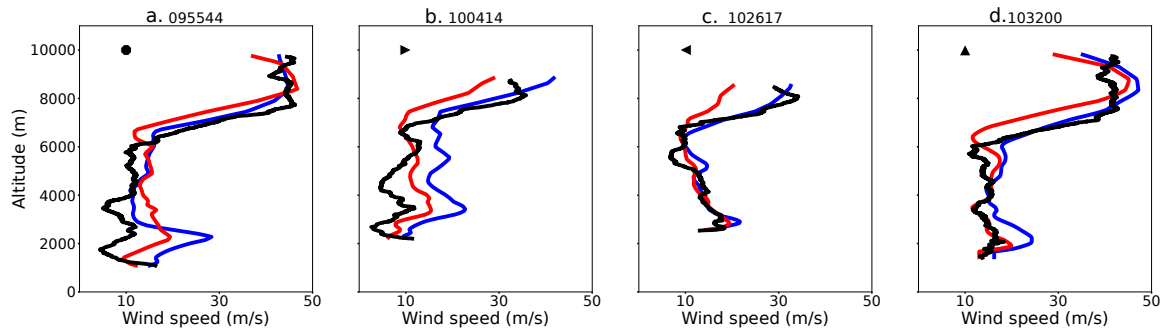
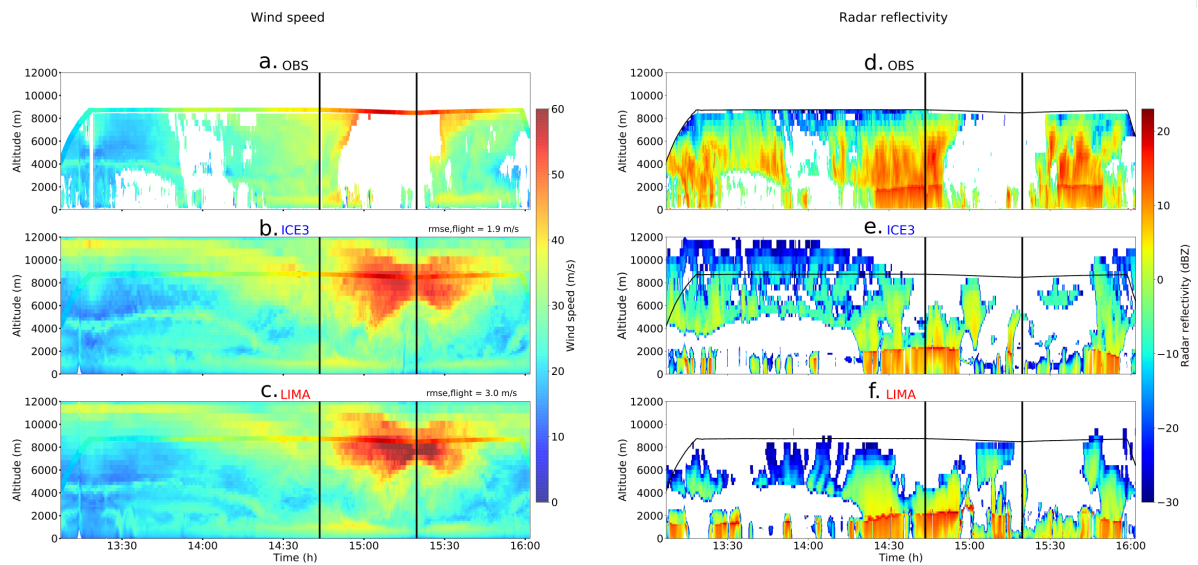


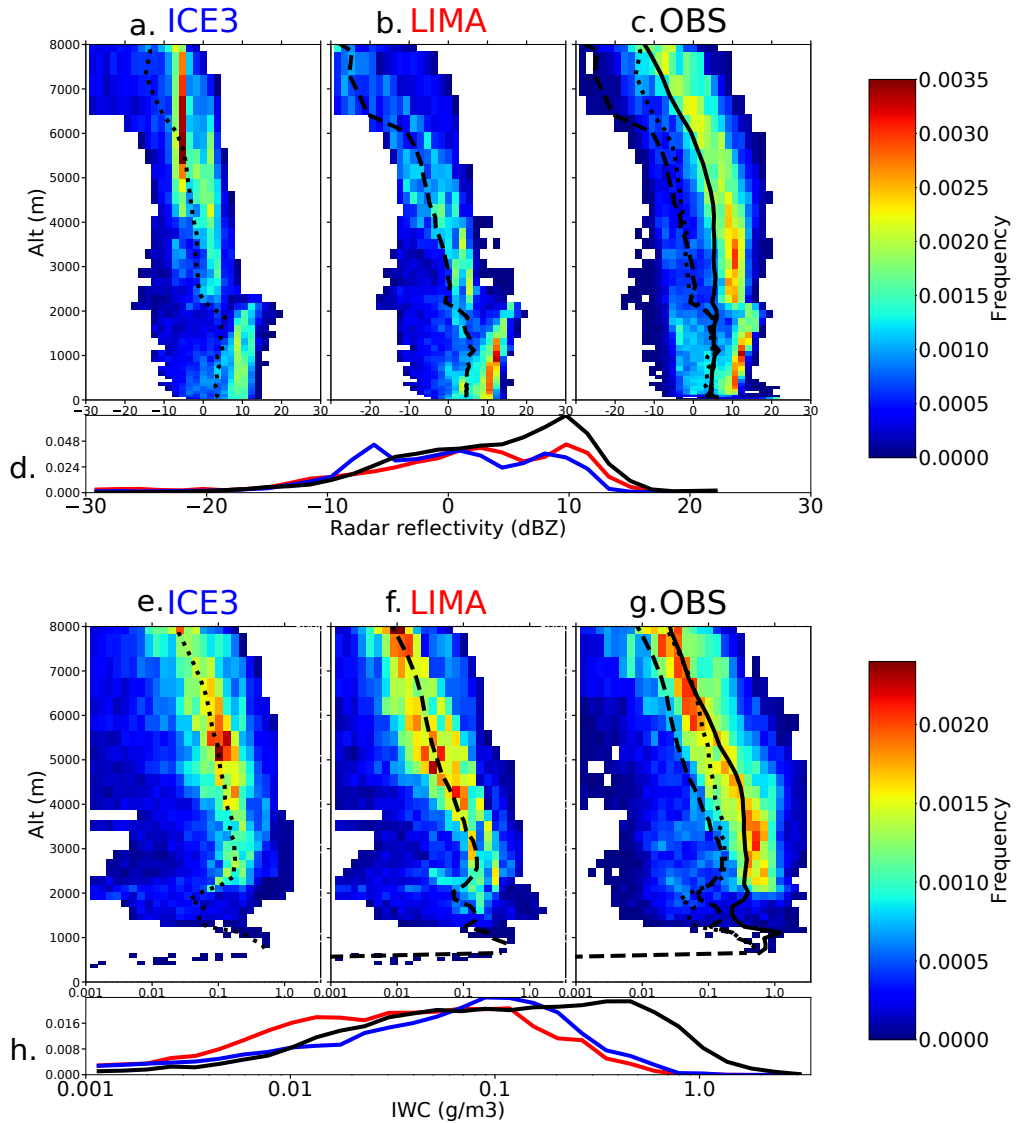
Figure 9. Brightness temperature at 10.8 μm at 12 UTC 2 Oct 2016 for the (a) ICE3, (b) LIMA and (C) the MSG observation. The black lines represent the two flight tracks.



985 Figure 10. Wind speed as observed (in black) from the 4 westernmost dropsondes launched during F6 over Greenland coast
 986 (see symbols in Figs. 4 or 9 indicating the launch location for each dropsonde) and simulated with ICE3 (in blue) and LIMA (in
 987 red). Each dropsonde is labelled according to the launch time using the format hhmss.



988 Figure 11. (a)-(c) Horizontal wind speed and (d)-(f) reflectivity along flight F7 (see bottom triangle in Fig. 9) for (upper panels)
 989 RASTA observations, (middle panels) ICE3 simulation, and (lower panels) LIMA simulation. The vertical dark lines stand for the
 990 time where the flight changed direction. Wind speed as measured by the in-situ aircraft instrument at the flight level are added on
 991 (a)-(c) with the same color bar. The RASTA data are regridded onto the Meso-NH grid.



992 Figure 12. Bivariate PDFs as a function of altitude of (a)-(c) reflectivity and (e)-(g) Ice Water Content for (a),(e) ICE3, (b),(f)
 993 LIMA and (c),(g) the observations regridded onto the model grid, mean vertical profiles are indicated for ICE3 (dotted line), LIMA
 994 (dashed line), and observations (solid line). The measurements and observations are normalized with the total number of points.
 995 Panels (d) and (h) correspond to the sum over height of the bivariate PDFs of reflectivity and IWC respectively with ICE3 (in blue),
 996 LIMA (in red) and observations (in black).